IJOER
RESEARCH JOURNAL

ISSN
2395-6992

International Journal of Engineering Research & Science

www.ijoer.com
www.adpublications.org

Volume-4! Issue-2! February, 2018 www.ijoer.com ! info@ijoer.com

Preface

We would like to present, with great pleasure, the inaugural volume-4, Issue-2, February 2018, of a scholarly journal, *International Journal of Engineering Research & Science*. This journal is part of the AD Publications series *in the field of Engineering, Mathematics, Physics, Chemistry and science Research Development*, and is devoted to the gamut of Engineering and Science issues, from theoretical aspects to application-dependent studies and the validation of emerging technologies.

This journal was envisioned and founded to represent the growing needs of Engineering and Science as an emerging and increasingly vital field, now widely recognized as an integral part of scientific and technical investigations. Its mission is to become a voice of the Engineering and Science community, addressing researchers and practitioners in below areas

Chemical Engineering	
Biomolecular Engineering	Materials Engineering
Molecular Engineering	Process Engineering
Corrosion Engineering	
Civil Engineering	
Environmental Engineering	Geotechnical Engineering
Structural Engineering	Mining Engineering
Transport Engineering	Water resources Engineering
Electrical Engineering	
Power System Engineering	Optical Engineering
Mechanical Engineering	
Acoustical Engineering	Manufacturing Engineering
Optomechanical Engineering	Thermal Engineering
Power plant Engineering	Energy Engineering
Sports Engineering	Vehicle Engineering
Software Engineering	
Computer-aided Engineering	Cryptographic Engineering
Teletraffic Engineering	Web Engineering
System Engineering	
Mathematics	
Arithmetic	Algebra
Number theory	Field theory and polynomials
Analysis	Combinatorics
Geometry and topology	Topology
Probability and Statistics	Computational Science
Physical Science	Operational Research
Physics	
Nuclear and particle physics	Atomic, molecular, and optical physics
Condensed matter physics	Astrophysics
Applied Physics	Modern physics
Philosophy	Core theories

Chemistry	
Analytical chemistry	Biochemistry
Inorganic chemistry	Materials chemistry
Neurochemistry	Nuclear chemistry
Organic chemistry	Physical chemistry
Other Engineering Areas	
Aerospace Engineering	Agricultural Engineering
Applied Engineering	Biomedical Engineering
Biological Engineering	Building services Engineering
Energy Engineering	Railway Engineering
Industrial Engineering	Mechatronics Engineering
Management Engineering	Military Engineering
Petroleum Engineering	Nuclear Engineering
Textile Engineering	Nano Engineering
Algorithm and Computational Complexity	Artificial Intelligence
Electronics & Communication Engineering	Image Processing
Information Retrieval	Low Power VLSI Design
Neural Networks	Plastic Engineering

Each article in this issue provides an example of a concrete industrial application or a case study of the presented methodology to amplify the impact of the contribution. We are very thankful to everybody within that community who supported the idea of creating a new Research with IJOER. We are certain that this issue will be followed by many others, reporting new developments in the Engineering and Science field. This issue would not have been possible without the great support of the Reviewer, Editorial Board members and also with our Advisory Board Members, and we would like to express our sincere thanks to all of them. We would also like to express our gratitude to the editorial staff of AD Publications, who supported us at every stage of the project. It is our hope that this fine collection of articles will be a valuable resource for *IJOER* readers and will stimulate further research into the vibrant area of Engineering and Science Research.

Mukesh Arora

(Chief Editor)

Board Members

Dr. S.R.Boselin Prabhu

Ph.D, Wireless Sensor Networks, M.E. Network Engineering, Excellent Professional Achievement Award Winner from Society of Professional Engineers Biography Included in Marquis Who's Who in the World (Academic Year 2015 and 2016). Currently Serving as Assistant Professor in the department of ECE in SVS College of Engineering, Coimbatore.

Dr. Maheshwar Shrestha

Postdoctoral Research Fellow in DEPT. OF ELE ENGG & COMP SCI, SDSU, Brookings, SD Ph.D, M.Sc. in Electrical Engineering from SOUTH DAKOTA STATE UNIVERSITY, Brookings, SD.

Zairi Ismael Rizman

Senior Lecturer, Faculty of Electrical Engineering, Universiti Teknologi MARA (UiTM) (Terengganu) Malaysia Master (Science) in Microelectronics (2005), Universiti Kebangsaan Malaysia (UKM), Malaysia. Bachelor (Hons.) and Diploma in Electrical Engineering (Communication) (2002), UiTM Shah Alam, Malaysia

Dr. D. Amaranatha Reddy

Ph.D.(Postdocteral Fellow,Pusan National University, South Korea), M.Sc., B.Sc. : Physics.

Dr. Dibya Prakash Rai

Post Doctoral Fellow (PDF), M.Sc.,B.Sc., Working as Assistant Professor in Department of Physics in Pachhuncga University College, Mizoram, India.

Dr. Pankaj Kumar Pal

Ph.D R/S, ECE Deptt., IIT-Roorkee.

Dr. P. Thangam

BE(Computer Hardware & Software), ME(CSE), PhD in Information & Communication Engineering, currently serving as Associate Professor in the Department of Computer Science and Engineering of Coimbatore Institute of Engineering and Technology.

Dr. Pradeep K. Sharma

PhD., M.Phil, M.Sc, B.Sc, in Physics, MBA in System Management, Presently working as Provost and Associate Professor & Head of Department for Physics in University of Engineering & Management, Jaipur.

Dr. R. Devi Priya

Ph.D (CSE),Anna University Chennai in 2013, M.E, B.E (CSE) from Kongu Engineering College, currently working in the Department of Computer Science and Engineering in Kongu Engineering College, Tamil Nadu, India.

Dr. Sandeep

Post-doctoral fellow, Principal Investigator, Young Scientist Scheme Project (DST-SERB), Department of Physics, Mizoram University, Aizawl Mizoram, India- 796001.

Mr. Abilash

MTech in VLSI, BTech in Electronics & Telecommunication engineering through A.M.I.E.T.E from Central Electronics Engineering Research Institute (C.E.E.R.I) Pilani, Industrial Electronics from ATI-EPI Hyderabad, IEEE course in Mechatronics, CSHAM from Birla Institute Of Professional Studies.

Mr. Varun Shukla

M.Tech in ECE from RGPV (Awarded with silver Medal By President of India), Assistant Professor, Dept. of ECE, PSIT, Kanpur.

Mr. Shrikant Harle

Presently working as a Assistant Professor in Civil Engineering field of Prof. Ram Meghe College of Engineering and Management, Amravati. He was Senior Design Engineer (Larsen & Toubro Limited, India).

Table of Contents

Synthesis and Use of Polyoxychloropropylen-Epoxymethacrylate Oligoesters as Active Modifier of Epoxy Diane Resin Ed-20

R.I.Ismailova[1], A.M.Mustafayev[2], N.Ya.Ishenko[3], I.A.Guseinov[4], B.A.Mamedov[5]

Institute of Polymer Materials of Azerbaijan National Academy of Sciences, Azerbaijan

Abstract— *The synthesis of polyoxychloropropylenepoxymethacrylate oligoesters by esterification of polyoxychloropropylenetriepoxide by methacrylic acid has been carried out. It has been established that by varying the conditions of carrying out of the reaction, one can prepare, mainly, the mono-, di- and trimethacrylic oligoesters. On the basis of epoxy diane ED-20 and synthesized polyoxychloropropylenepoxymethacrylate oligoesters as modifiers there have been prepared the self-extinction compositions, which after curing by N, N[1]–diaminodiphenylsulfone possess higher physical-mechanical, adhesion and heat-physical properties.*

Keywords— polyoxychloropropylenetriepoxide, ED-20, diaminodiphenylsulfone, methacrylic acid, epoxymethacrylate, methacrylate oligoesters, self-extinction compositions.

I. INTRODUCTION

The epoxymethacrylates prepared by esterification of epoxy-containing oligomers by methacrylic acid find wide application as the photo- and radiation-sensitive components and also as the modifiers of epoxide resins [1, 2]. Their use as the low-viscous plasticizers and reactive modifiers allows preparing the polymer materials with low residual tension, higher elasticity, high adhesion and impact strength. Most often, the composition containing oligoestermethacrylates as a modifier at structuring are chemically not connected with molecules of epoxy resin [3]. This leads to deterioration of some indices of the prepared polymer materials and first of all – to decrease of stability in the conditions of long exploitation. From this point of view the epoxymethacrylate oligoesters synthesized by esterification of polyoxychloropropylentriepoxide (1) by methacrylic acid are of interest. An availability of chlorine atom in composition of these compounds allows their use as antipyrenes and an availability of epoxide groups along with methacrylate fragments leads to the chemical binding with modifying epoxide resin during curing of the prepared mixture with curing agents of amine type.

II. EXPERIMENTAL

Polyoxychloropropylenetriglycidyl ester (I) has been synthesized on methodology given in [4, 5].

2.1 Interaction of polyoxychloropropylenetriglycidyl ester with methacrylic acid

a**)** 0,05 mol of polyoxychloropropylenetriglycidyl ester, 0.15 mol % of pyridine (from total quantity of reagents), 50 ml of toluene were placed in three-necked flask equipped with mechanical mixer, thermometer, reflux condenser and dropping funnel and were added on dropwise 0.0125 mol of freshly distilled methacrylic acid dissolved in 20 mi of toluene. The reaction temperature spontaneously raised to 313 K. Then for 3,5 h the reaction temperature was raised to 343 K. After completion the reaction mass was washed with water to neutral medium and extracted by toluene. After drying over Na_2SO_4 distillation of solvent the prepared product was separated by column chromatography (Al_2O_3, solvent – hexane-ethylacetate 40:1). Two fractions have been isolated, the first fraction – 5.7 g (83.8%), n_D^{20} =1.4790. Found, % : C 47.65, H 6.14, Cl 16.69, $C_{25}H_{41}O_{11}Cl_3$(II). Calculated, % C 48.09, H 6.57, Cl 17.07. The second fraction: 0.81 g (11.9%), n_D^{20} = 1.4730. Found, % : C 48.72, H 6.91, Cl 14.75. $C_{29}H_{47}O_{13}Cl_3$ (III). Calculated, % C 49.04, H 6.62,Cl 15.01.

b**)** Similarly to method (a) 0.05 of polyoxychloropropylenetriglycidyl ester, 0.025 mol of methacrylic acid, 30 ml of toluene and 0.0125 mol. % (from total quantity of reagents) of pyridine was heated at 365 K for 5h. On completion of the reaction the products were separated by column chromatography. Two fractions have been isolated: the first of them is completely identical to product III prepared on method (a), a yield is 15.4 g (86.8%), n_D^{20} =1.4790. Found, %: C 48.61, H 6.17, Cl 14.70, $C_{29}H_{47}O_{13}Cl_3$ (III). Calculated, % C 49.04, H 6.62, Cl 15.01. The second fraction: 3.6 g (8.9%), n_D^{20} =1.4685. Found, % : C 49.34, H 6.26, Cl 12.87. $C_{33}H_{53}O_{15}Cl_3$ (IV). Calculated, % C 49.78, H 6.66, Cl 13.38.

c) 0.15 mol of methacrylic acid was added to solution of 0.05 mol of polyoxychloropropylenetriglycidyl ester in 50 ml of toluene, 0.0125 mol % (from total quantity of reagents) of pyridine and was heated at 365 K for 5 h. On completion of the reaction products were separated by column chromatography. The isolated product (37.5 g, 94.2%) on physical-mechanical indices coincides completely with compound IV prepared on methodology (b).

d) The compositions were made by intensive mixing the calculated quantities of ED-20 and modifier to complete homogeneity on water bath (363-373 K) and then the curing agent (DADPhS) was introduced to the system. After complete dissolution of components, the composition was degased under vacuum and poured in fluoroplastic forms necessary for preparation of the samples in accordance with intended tests. The compositions after keeping at room temperature for 24 h was subjected to thermocuring. Curing mode: at 393 K – 3 h, at 423 K – 3 h, at 483 K – 5 h. A degree of curing of the compositions was estimated by extraction of their crushed samples by acetone in Soxhlet apparatus for 8-10 h. In the tested samples a degree of curing was no less 96-98%. In the identical conditions there have been made the compositions ED-20 / DADPhS for comparison.

The test of the samples was carried out on tensile testing machine of pendulum type FMPW-500 with movement rate of the lower clamp 30 mm/min. The average-arithmetical values of five measurements have been taken as the results of the tests.

e**)** The curing reaction of composition has been studied by a method of thermal analysis on derivatograph of system "Paulik-Paulik-Erdei". Weighting of the studied sample – 200 mg, sensitivity of the channels TGA-200 and sensitivity of galvanometer DTA-250 μν and DTG-1 μν, temperature rise rate – 5 deg./min. in air current.

f) The thermooxidative destruction of the cured epoxide compositions was also studied by derivatographic method on derivatograph of system "Paulik-Paulik-Erdei" at dynamic regime in air current. Temperature rise rate – 5 deg./min. The sensitivity of the channels TGA-200 μν, galvanometer DTA-250 μν and DT-1 μν. Weighting of the samples – 200 mg. The heat-resistance of the cured samples was determined on Vicat device, load – 5 kg.

g) The IR-spectra of substances in vaseline oil were taken on spectrometer "UR-20". The NMR^{1}H-spectra were registered on spectrometer "Bruker-300" (300MHz) for solutions in deuterated acetone. Internal standard – HMDS.

III. RESULTS AND DISCUSSION

This work has been devoted to the preparation and investigation of modifying influences of properties of epoxymethacrylate oligoesters on the basis of polyoxychloropropylenetriepoxide compound (I) synthesized on method described in [4-7]. The esterification of polyoxychloropropylenetriepoxide oligoester by methacrylic acid was carried out in a medium of toluene in the presence of pyridine (0,15 mol. % from total quantity of reagents).

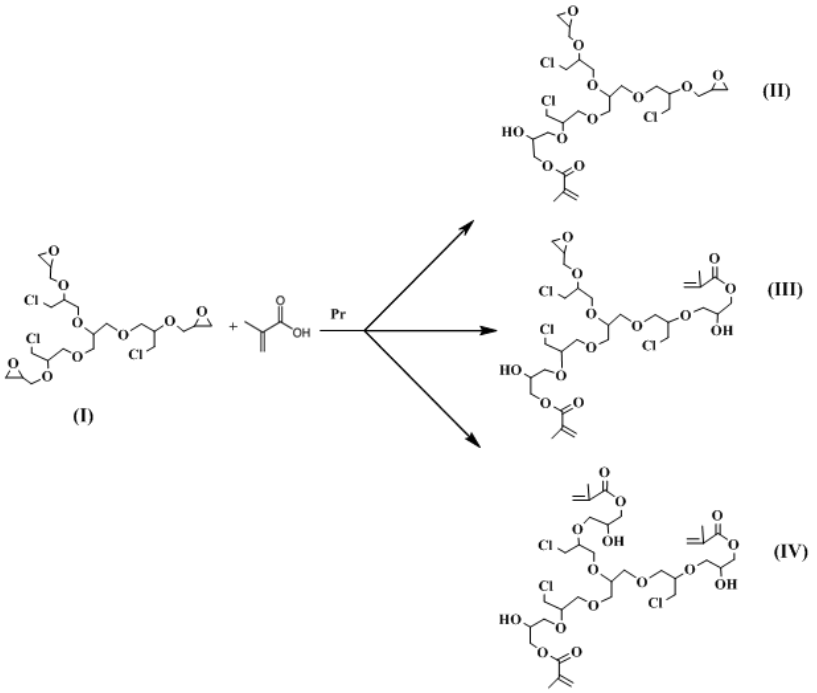

The reaction course was controlled on consumption of methacrylic acid by a method of acid-base titration (0,1 n. aqueous solution KOH, indicator – bromthymol blue). The results of the carried out experiments showed that a degree of conversion and ratio of the prepared reaction products depend on molar ratio of the initial reagents, temperature and reaction duration. For quantitative estimation and isolation as individual view of the reaction products with the aim of their identification and subsequent analysis it was used the column chromatography on aluminum oxide with use of hexane-ethyleacetate as eluent of mixture (40:1). Under optimal conditions the yields of corresponding epoxymethacrylates are 85-93%.

The structure of the synthesized compounds has been confirmed by the methods of IR- and PMR-spectroscopy. In the IR-spectra of the compounds II-IV there are absorption bands at 1620 cm^{-1}, stipulated by valence vibration of double bond. The absorption bands at 1180 and 724-748 cm^{-1}evidence about availability of C-O-C and C-Cl- bonds, and the band at 1715 cm^{-1} is characteristic for valence vibrations of carbonyl group in ester fragments. The weak bands at 915 cm^{-1} in the IR-spectra of the compounds II, III correspond to vibrations of epoxide ring. An availability of the wide absorption band about 3460 cm^{-1} confirms an appearance of the secondary hydroxyl groups in the compounds II-IV [8].

In the PMR-spectra of the synthesized compounds along with signals of protons of the initial compound (I) there are the signals of methyl group (1.75 ppm), multiplet of protons in double bond (5.2 ppm), the signals of protons of methylene group in ester fragment (4.16 ppm). A group of the signals of small intensity in the field of 2.64-2.73 ppm refers to the signals of residual epoxide groups in the compounds II, III [9].

The synthesized polyoxychloropropylenepoxymethacrylates (II-IV) were used as modifier of the epoxide composition on the basis of ED-20. N, N^1– diaminodiphenylsulfone (DADPhS) was used as a curing agent. It was known that for development of the qualitative epoxide compound it is necessary to choose the optimal quantity of curing agent, modifying addition and to find the optimal regime of curing. The optimal quantity of the compounds (II-IV) used as modifier have been determined experimentally and controlled by mass loss on curves TGA and DTA. The curing reaction proceeds in the field of 353-473K, about which an exopeak of curing on DTA curve evidences.

The obtained results evidence that on DTA curves there are appeared two exopeaks in the temperature interval 393-488 K (Fig.1).

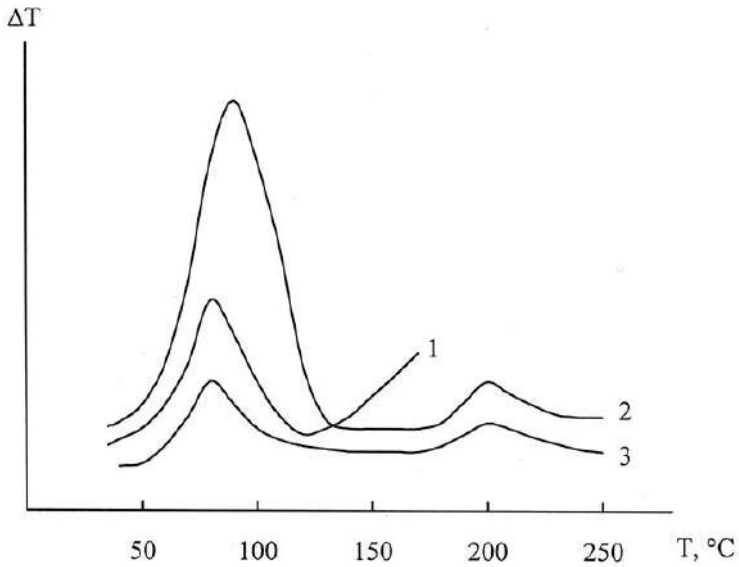

FIGURE 1 – DTA CURVES OF CURING OF SYNTHESIZED RESINS AND ED-20 WITH:
1 – ED-20 EPOXIDE RESIN;
2 – POLYOXYCHLOROPROPYLENEPOXYMETHACRYLATE OLIGOMER;
3 – POLYOXYCHLOROPROPYLENEPOXYMETHACRYLATE.

The obtained experimental data evidence that in the compositions cured at high temperatures the internal defects are formed. In this connection, for realization of curing process at relatively low temperatures an accelerator UP 606/2 2,4,6-tris (dimethylaminomethyl phenol) was introduced in reaction mixture. In these cases, two exopeaks on DTA curves in curing process of the compositions are also observed, and the first of them is displaced to more low temperature field.

It has been established that the observed exopeak at 363 K has been connected with curing with participation of epoxide groups, and the second exopeak at 473 K characterizes a conversion proceeding with participation of double bond of modifying oligomers (interaction with amine of group of curer or its fragment and thermal polymerization). Indeed, during carrying out of curing process of system ED-20 + triglycidyl ester of propantriol + curing agent on DTA curve an exopeak at 473 K is not observed and only one exopeak at 363 K is appeared.

The thermal stability of the prepared compositions was estimated on values of temperature corresponding to 10%, 20% and 50% mass loss of the samples and on activation energy value of decay calculated on TGA curve by a method of double logarithm. The obtained data are presented in Table 1.

TABLE 1
THERMAL CHARACTERISTIC OF CURED EPOXIDE COMPOSITIONS PREPARED WITH USE OF COMPOUNDS II AND III AS A MODIFIER

Composition, mass.p.	T_{10}	T_{20}	T_{50}	Polydecay period, T ½, min.	E of decay kJ/mol
ED-20-100 DADPhS-20 Modif.(II)-10	150	180	290	40	63.52
ED-20-100 DADPhS-20 Modif.(II)-20	180	210	330	48	69.87
ED-20-100 DADPhS-20 Modif.(II)-30	130	170	260	37	60.21
ED-20-100 DADPhS-20 Modif.(III)-10	180	200	300	35	95.8
ED-20-100 DADPhS-20 Modif.(III)-20	210	225	350	55	115.82
ED-20-100 DADPhS-20 Modif.(III)-30	120	180	280	40	65.4

As is seen from results presented in Table the optimal quantity of modifier is 20 mass p. per 100 mass p. of epoxy diane resin, at such ratio of components the best thermal stability of cured composition material is reached. It should be noted that the modification of epoxide resin by compound (III) leads to a formation of more thermostable materials, which has been apparently connected with availability of two epoxide groups in one molecule of the compound III and as a result with formation of more thick-cross-linked structure in the curing process.

The dependence of some physical-mechanical indices of epoxide compounds modified (II-IV) is presented in Table 2.

As is seen from obtained data, the physical-mechanical properties of the cured epoxide compositions with participation of modifiers II-IV are essentially higher than such ones for compositions ED-20:curer. An increase of a quantity of modifier in all samples of the compositions to 30 mass p. although leads to essential increase of deformation properties, however the strength properties of the compositions reach maximum at content 20 mass p. of modifier. A heat-resistance of modified compositions is considerably higher than in unmodified ones, and an availability of chloromethyl groups gives self-extinction to compositions. The results of the experiments evidence about that the modifier containing both hydroxyl and methacrylic groups in its composition immediately influences on formation process of net structure of cured material. As the authors have

shown [10], in the polycondensated processes at formation of three-dimensional net and availability of hydroxyl group not only increases a reactivity of oligomers but actively influences on process direction.

TABLE 2

PHYSICAL-MECHANICAL INDICES OF COMPOSITIONS ED-20/MODIFIER (II-III) OF THE VARIOUS COMPOSITION CURED BY DADPHS (ACCELERATOR – UP-606 / 2)

Ratio of ED-20: modifier: curing agent, mass.p.	Ultimate strength (MPa) at			Adhesion to steel, MPa	Relative elongation, %	Vicat heat-resistance, ^{0}C	Burning time of the sample after fire removal, sec.
	tension	flexure	com-pression				
Modifier (II)							
90:10:20	77	142	147	20	3.5	165	17
80:20:20	84	151	161	24	6.3	157	Damps
70:30:20	73	127	143	17	13.4	121	Damps
Modifier (III)							
90:10:20	80	149	156	21	3.4	175	21
80:20:20	90	161	165	26	6.5	163	Damps
70:30:20	78	141	144	17	13.7	125	Damps
Modifier (IV)							
90:10:20	84	154	159	20	3.7	163	21
80:20:20	91	165	164	26	6.5	154	Damps
70:30:20	79	135	147	19	13.8	120	Damps
ED-20: DADPhS							
100:20	51±4	121+5	140	14	2.3	119	Burns

Among modifiers II-IV the compound III as a result of the most successful combination of epoxide, hydroxyl and methacrylic groups showed the best and stable results in the compositions with DADPhS.

The improvement of heat-physical, deformation and strength properties of the prepared compositions on the basis of ED-20 and modifying oligomers of II-IV has been connected with active participation of epoxide, hydroxyl and double bonds in formation of effective net structure. At the initial stage of curing the epoxide groups of modifier react actively (at 80-90°C on DTA curve an exopeak is appeared), and at the deep stages the double bonds of modifier molecule or their fragments in the composition of macromolecule undergo the reaction with amine group of curing agent or thermal polymerization. As a result more thick-cross-linked structures are formed and the cross-linked areas are basically formed from molecules of modifying oligomer and possess more high elasticity. An availability of such net structure stipulates an improvement of the above-mentioned exploitation indices of the developed composition materials.

Thus, the obtained results evidence about that the compounds II-IV used as modifier-antipyerene partcipate actively in the process of formation of set structure in the epoxide compositions, provide them high physical-mechanical, heat-physical and adhesion indices and give self-extinction to compositions.

IV. CONCLUSIONS

Polyoxychloropropylenepoxymethacrylate oligoesters by esterification of polyoxychloropropylenetriepoxide of methacrylic acid have been synthesized. It has been shown that by varying the conditions of carrying out of the reaction, one can prepare, mainly, the mono-, di- and trimethacrylic oligoesters.

On the basis of epoxy diane ED-20 and synthesized polyoxychloropropylenepoxymethacrylate oligoesters as modifiers there have been prepared the self-extinction compositions, which after curing by N, N^1–diaminodiphenylsulfone possess higher physical-mechanical, adhesion and heat-physical and thermal properties.

REFERENCES

[1] A. Berlin, G. V. Korolev, T. Ya. Kofeli, Yu. M. Sivergin, Aryl oligomers and materials on their base. M.: Khimiya, 1983, 232 p.

[2] Yu. M. Sivergin, S. M. Usmanov, Synthesis and properties of oligoester(meth)acrylates. M.: Khimiya, 2000, 420 p.

[3] S. Freydin, Strength and durability of glue compounds. M.: Khimiya, 1971, 276 p.

[4] M. Mustafayev, N. A. Alekperov, S. J. Murshudova, "Some peculiarities of synthesis and properties of chlorine-containing oligoesters on the basis of propantriol and 3-chloro-1,2-epoxy propane," Azerb. Chem. J., pp. 127-131, February 2006.

[5] M. D. Korolkova, L. S. Masliy, N. A. Petrov, L. N. Khludova, R. G. Pomyanek, N. I. Lebedeva, "Method of preparation of chlorine-containing aliphatic epoxides, " Auth. Cert. USSR 416368, 1974.

[6] M. Mustafayev, S. J. Murshudova, "Flame- retardant chlorine- containing aliphatic epoxide resins," XVIII Ulusal Kimya Kongresi, p. 1005, Kars, Turkiye, 2004.

[7] M. Mustafayev, S. J. Murshudova, N. A. Alekperov, "Self-extinction unsaturated epoxymethacrylates on the basis of polyoxypropylene-triepoxide, " Abstracts of VI Baku International Conference on Petrochemistry devoted to 100 anniversary of the Academician Yu. G. Mamedaliyev, p. 162, Baku, 2005.

[8] L. Bellami, New data on IR-spectra of complex molecules. M.: Mir, 1971, 318 p.

[9] D. Emeli, D. Finey, L. Satklif, NMR-spectroscopy of high resolution, vol. 2. M.: Mir, 1969, p. 452.

[10] Physico-chemistry of multicomponent polymer systems / Edited by Yu. S. Lipatov, vol. 2. Kiyev: Naukowa dumka, 1986, pp. 68-137.

Influence of Y_2O_3 on the structure of Y_2O_3-doped $BaTiO_3$ powder and ceramics

Ana María Hernández-López[1], Sophie Guillemet-Fritsch[2], Zarel Valdez-Nava[3], Juan Antonio Aguilar-Garib[4], Christophe Tenailleau[5], Pascal Dufour[6], Jean-Jacques Demai[7], Bernard Durand[8]

[1]CICFIM, Universidad Autónoma de Nuevo León, San Nicolás de los Garza, N.L., MX 66455.
[1,2,5,6,7,8]CIRIMAT, Université de Toulouse, CNRS, Université de Toulouse 3-Paul Sabatier,118 route de Narbonne, 31062, Toulouse Cedex 9, France.
[3]LAPLACE, Université de Toulouse, CNRS, INPT, UPS, France.
[4]Universidad Autónoma de Nuevo León, FIME, San Nicolás de los Garza, N.L., MX 66455.

Abstract*—Barium titanate ($BaTiO_3$) doped with rare-earth elements (REE) is used as dielectric in the manufacture of multilayer ceramic capacitors (MLCCs). The most common REE oxide employed as dopant for this application is Y_2O_3. The behavior of the Y^{3+} in the $BaTiO_3$ structure depends on its concentration and the sintering conditions, among other factors, which can induce the formation of secondary phases that are a potential cause a detriment to the electrical properties of $BaTiO_3$. The purpose of this work is to perform a phase characterization of $BaTiO_3$ doped with different concentrations of Y_2O_3, validating its possible contribution to the formation of secondary phases. The role of Y_2O_3 was evaluated on two kinds of raw materials. The first one is pure $BaTiO_3$ (< 100 ppm Y) and the second kind is a commercial formulation designed for MLCCs known as X7R (-55°C and 125°C, 15% tolerance), which among other elements, already contained 1 wt% of Y_2O_3. High concentrations of Y_2O_3 (1% up to 20 wt%) were used aiming to promote structural changes, and even the formation of secondary phases in amounts suitable to be detected by X-ray diffraction. Heat treatment of powder and sintering of ceramics (powder compacted at 2 MPa) were conducted in air (1310°C in air for 3 h, two steps: 1350°C then 1150°C 15 h). A phase transition from tetragonal to a mixture of tetragonal and cubic was observed as Y_2O_3 concentration increases in the thermally treated powder and in the corresponding ceramics. Commercially formulated powder showed higher densification than pure $BaTiO_3$, and produced cubic structure at higher Y_2O_3concentrations. The phase $Ba_6Ti_{17}O_{40}$is detected in the 20 wt% Y_2O_3-doped sample.*

Keywords*—*$BaTiO_3$, doping, Y_2O_3.

I. INTRODUCTION

$BaTiO_3$ presents interesting electromagnetic properties and has become the main component of the formulation of the dielectric material for multilayer ceramic capacitors (MLCCs) [1, 2]. The formulation used in this application must be designed to control the electromagnetic properties of the layer, especially at high temperature and under high electric field [3,4]. For this purpose, several additives and dopants are added to $BaTiO_3$. They include cations such as Mn, Mg and Ca, that can partially compensate the electrons and holes that the system might contain,due to the presence of oxygen vacancies [3, 5]. They also include sintering aids, such as SiO_2, which reduce the sintering temperature. Indeed, it has been reported that SiO_2 leads to formation of a liquid phase from the ternary system BaO-TiO_2-SiO_2, diminishing the eutectic point from 1320°C to near 1260 °C [6,7]. Finally, REE are added, Dy^{3+}, Ho^{3+}, Sm^{3+}, La^{3+}, Yb^{3+}or Y^{3+}. They substitute Ba and Ti cations in the $BaTiO_3$ structure [8, 9]. However, in particular, Dy^{3+}, Ho^{3+} and Y^{3+}, have shown an amphoteric behavior (occupying A- or B-site) and they are described as helpful for the lifetime of the MLCCs [1]. Y_2O_3 is commonly employed as dopant in the commercial formulation of powder for fabrication of MLCCs, because at industrial scale. It results in similar properties than adding Ho_2O_3, Er_2O_3 or Dy_2O_3, and it is less expensive[8]. Dopants also take part in the formation a so-called "core-shell" structure that is claimed to contribute to the temperature stability of the dielectric properties [8-11]. Y_2O_3 ionic radius (0.107 nm) is intermediate between that of the Ba^{2+} ion (0.161 nm) and the Ti^{4+} ion (0.06 nm). Therefore Y^{3+}can take either Ba^{2+} or Ti^{4+} cation site in the $BaTiO_3$ lattice [1, 2], and can behave as acceptor or donor according to the position in the lattice. The energy required to form a Ti^{4+} vacancy in the $BaTiO_3$ lattice is 7.56 eV whereas it is only 5.94 eV to form a Ba^{2+} vacancy [12-14]. The partial pressure of oxygen and sintering temperature will also induce the formation of Ba^{2+}or Ti^{4+} vacancies, leading Y^{3+} to occupy either one or both of them [12, 14]. This will be influenced also by the Ba/Ti ratio, the dopant concentration and its solubility, which varies according to Y^{3+} taking either the Ba- or the Ti-site. Zhi et al. [15] indicated a solubility of Y^{3+}at the Ba-site of about 1.5 at% when sintering in air at 1440 – 1470°C, while it reaches 4 at%

when sintering under reducing conditions [16]. For the Ti-sites instead, the solubility is higher ≈12.2 at% at 1515°C when sintering in air.Wang et al. [2] reported that the introduction of Y^{3+}in the $BaTiO_3$ lattice, can lead to structural changes, as phase transformation from tetragonal to cubic. Also, it has been observed that the solid solubility of the dopant in the $BaTiO_3$ is surpassed, when secondary phases are formed as precipitates. In the case of Y^{3+}, Belous et al. [17]reported the formation of the $Ba_6Ti_{17}O_{40}$ and $Y_2Ti_2O_7$ as secondary phases. The pyrochlore phase $Y_2Ti_2O_7$ was evidenced byYoon et al. [3] and Zhang et al. [8] and they suspected that these phases are detrimental to the reliability of $BaTiO_3$-based MLCCs.

In most industrial processes the dopant level is below 1 wt% [12] and the sintering is performed in a reducing atmosphere. Whereas in this research, doping levels are much higher and sintering is carried out in air. To understand the role of Y^{3+} addition in the formation of second phases a large range of dopants levels need to be explored up to and above the solubility limit. In this work we aim to investigate the structural changes of $BaTiO_3$ structure when adding Y_2O_3, induced by high doping levels (>1 wt%) when sintering is performed under air.

II. MATERIALS AND METHODS

Powder of $BaTiO_3$ doped with Y_2O_3 was prepared (according to the formula $Ba_{1-x}Y_xTi_{1-x/4}O_3$) by traditional solid state reaction. Two types of $BaTiO_3$were used, "BT-A" with commercial reagent-grade purity (Ferro Electronic Materials Inc.), and "BT-B" with formulated composition for its application in MLCCs production, containing additives, mainly: Y_2O_3: 1.05%; SiO_2: 0.30%, CaO: 1.34%). Each $BaTiO_3$ powder was mixed with the necessary amount of Y_2O_3 to obtain doped samples at 2.5, 5 and 20 wt%, then they were ball-milled in a polyurethane mill bottle with yttrium-stabilized zirconia balls, using ethanol as the grinding media for 4h.

With the aim to observe any structural change induced by doping, the powder (x = 2.5 to 20 wt%) was thermally treated at 1310°C in air atmosphere for 3h. Ceramics were prepared with the powder containing 2.5 and 5 wt% Y_2O_3. Then the powder was dried, 1 wt% polyvinyl butyral (PVB) was added to the powder that were mixed, grinded and sieved. Finally it was compacted using uniaxial pressing, producing discs of 8 mm in diameter. The green discs were sintered in air using a tube furnace, under a two-step sintering protocol which reached 1350°C and then remained at 1150°C for 15 h.

The crystalline phase of powder and sintered samples was characterized by X-ray diffraction (XRD, Model D4 Endeavor, Bruker AXS), using the Cu-α (λ = 1.54 Å) radiation in the 2θ range 10 - 80°. The bulk density of the ceramics was determined from the samples mass and geometry. Powder morphology was analyzed by scanning electron microscopy (SEM, JSM-6510LV, JEOL). The particles size was determined from the micrographs using Image J software.

III. RESULTS AND DISCUSSION

The crystal structure and the densification of the different samples are shown in Table 1.

TABLE 1
IDENTIFICATION, CHEMICAL COMPOSITION AND STRUCTURE OF THE STUDIED SAMPLES

$BaTiO_3$ raw material	Y_2O_3 wt%	Sample ID	Crystalline structure[a]		Secondary phase	Densification (%)
			Powder	Ceramic		
BT-A (reagent-grade)	0	A0	T	T	--	93.7
	2.5	A2.5	T	T+C	--	60.8
	5	A5	T	T+C	--	61.0
	20	A20	T+C	--	--	--
BT-B (commercially formulated)	1	B1	T	T+C	--	96.2
	2.5	B2.5	T+C	C	--	80.1
	5	B5	T+C	C	--	72.6
	20	B20	T+C	--	$Ba_6Ti_{17}O_{40}$	--

[a]*Preponderant phase. T: Tetragonal; C: Cubic.*

3.1 $BaTiO_3$Powder

SEM images of the undoped $BaTiO_3$ powder, A0 and B1, (Fig. 1 (a and c, respectively)) show that both powder present particles with a coarse-faceted morphology. Two sizes of particles are observed, a range of particles average size of 0.48μm and 1.25 μm for the A0 and of 0.46 μm and 0.81 μm for the B1. Although the values are close the maximum average value of the B1 particles is lower than the one of the A0 particles, which is due to the thermal treatment given to the formulated powder, as requirement for its use in the MLCCs production process. On the other hand, the SEM pictures of the 5 wt%

Y_2O_3-doped $BaTiO_3$ powder thermally treated (Fig. 1 (b and d)), show more spherical and defined particles, compared to the undoped powder. They present a more uniform size (A5: 0.58 µm and B5: 0.53 µm) and it is possible to observe aggregates, which might evidence an incipient sintering during the applied thermal process at 1310°C.

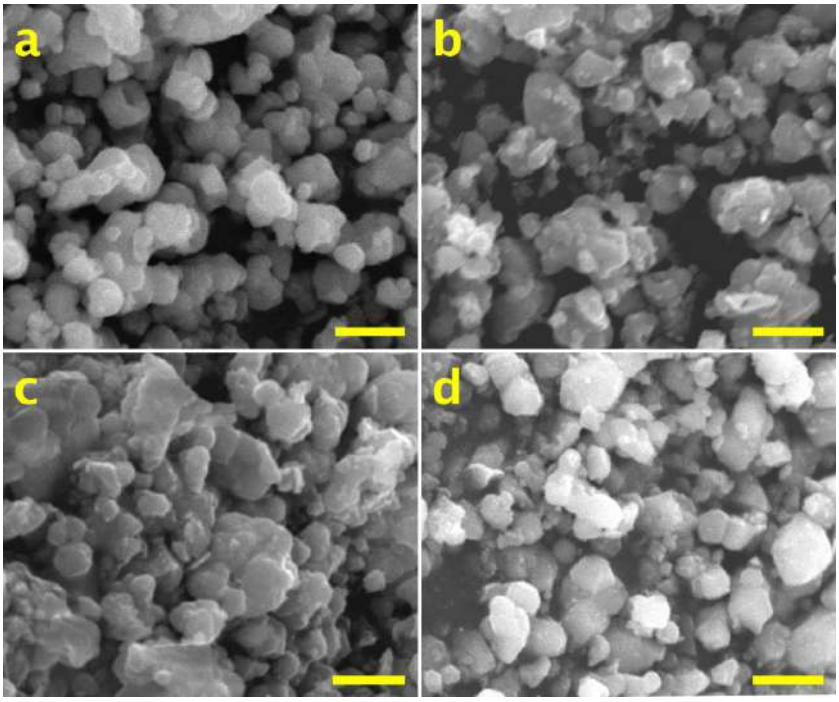

FIG. 1. SEM images of undoped $BaTiO_3$: (a) A0, (c) B1 and 5 wt% Y_2O_3 (TT): (b) A5, (d) B5 powder. (TT: Thermally treated). Scale bar: 1µm.

X-ray diffraction patterns corresponding to the thermally treated powder are presented in Fig.2. Diffraction patterns of powder obtained from the BT-A [(a) A0, A2.5, A5 and A20] fit well with the tetragonal phase. The insets in Fig. 2.a show the peaks associated to the (111) as well as (002)(200) planes of this phase. Further, on the inset of the diffraction peak at 2θ about 45°, the split in two peaks, is characteristic of a tetragonal phase [2]. For the A20 powder, the planes (002) and (200) suffer a slight distortion and the plane (111) shifts to a lower angle. Moreover for the A5 and A20 samples, the peaks corresponding to Y_2O_3 appear, meaning that at least a part of it remains free outside of the $BaTiO_3$ lattice, indicating that the solubility limit was surpassed. The shift to lower angles of some peaks is related to an expansion of the unit cell volume due to the substitution of Ba^{2+} by Y^{3+} ions.

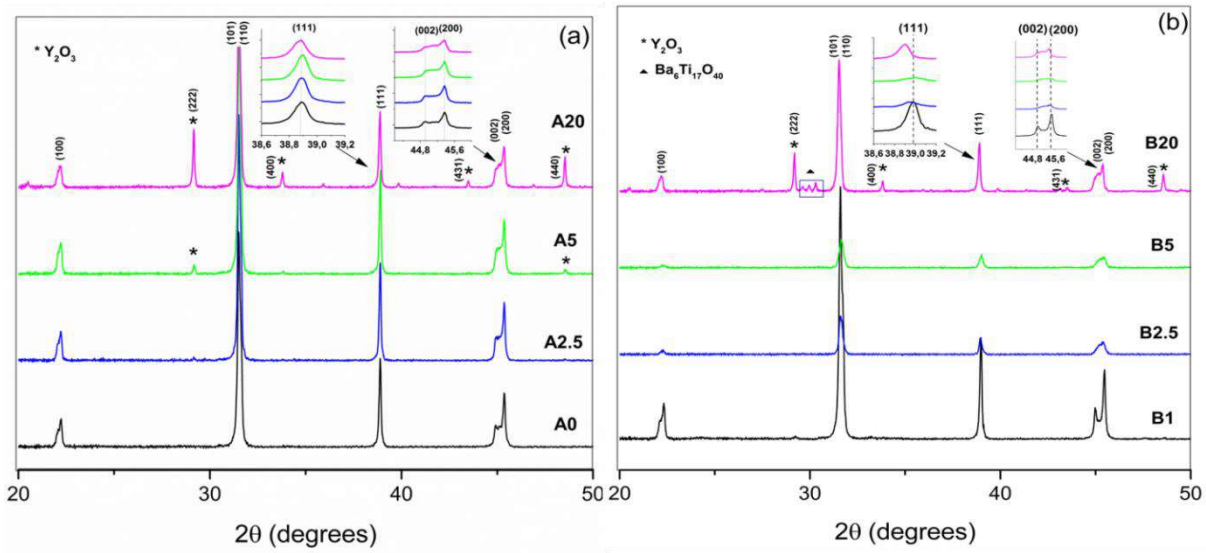

FIG. 2. X-ray diffraction patterns of undoped $BaTiO_3$ (1350°C) and Y_2O_3 - 2.5, 5 and 20 wt% - doped $BaTiO_3$ (1350°C) powder. Powder coming from (a) BT-A and (b) BT-B.

On the other hand, the XRD patterns corresponding to the BT-B powder show more changes according to the increasing Y_2O_3 concentration. In this case, the raw material already contains about 1 wt% of Y_2O_3. The pattern of powder B1 clearly shows a tetragonal phase, whereas those of powder B2.5, B5, and B20 evidence a mixture of tetragonal and cubic phases. For the B20 powder the split of (002) and (220) is more clear than for powder B2.5 and B5 and a shift to lower angle of the (111) peak is also noticed. Contrary to the A samples, the peaks corresponding to Y_2O_3 are detected only for the powder B20, implying the remaining of most of it as a free oxide. Moreover, for B20, three additional peaks appear between $2\theta \approx 29.5$ - 30°. They do not match with the $BaTiO_3$ nor with the Y_2O_3 phases. They could be attributed to the interaction of the Y_2O_3 excess with the $BaTiO_3$ matrix in conjunction with that of the additives already present. Considering the possible formation of secondary phases when the solubility of Y_2O_3 has exceed the limit of 1.5 at% for the Ba-site and 12.3 at% for the Ti-site (in air atmosphere) [15], a screening for secondary phases was made, finding a match with $Ba_6Ti_{17}O_{40}$ (JCPDS 35-0817). $BaTiO_3$and TiO_2 are likely to form a eutectic around 1320° - 1330°C and if SiO_2 is present, the eutectic point temperature decreases down to 1245° - 1260°C [18, 19]. Even without the presence of a liquid phase [20], the interaction between the dopants and the additives under our experimental conditions, could lead to a Ti-rich phase forming the secondary phase $Ba_6Ti_{17}O_{40}$. This second phase has been reported previously [14, 17].

3.2 $BaTiO_3$ Ceramics

Ceramics are prepared by sintering undoped and doped powder, BT-A (A0, A2.5, A5) and BT-B (B1, B2.5, B5), in the conditions described in the previous section.

Fig. 3 shows the X-ray diffraction patterns of the ceramics. The undoped ceramic (A0) crystallizes in a tetragonal phase, while the doped ones (A2.5 and A5) consist in a mixture of cubic and tetragonal perovskite phases as shown in the inset (Fig. 3(a)), zone around $2\theta \approx 45°$ where the split of the (200) peaks is deformed. The influence of the Y_2O_3 over the $BaTiO_3$ structure is greater in the case of the ceramics. Comparing the XRD pattern from the B1 powder (Fig. 2 (b)) and the corresponding ceramic (Fig. 3 (b)), it is possible to see (inset $2\theta \approx 45°$) that there is no peak splitting indicating a phase transformation from tetragonal to a cubic [10-12]. The same behavior is observed for B2.5 and B5 ceramics. This behavior points out the strong interaction between additives and dopants added to the $BaTiO_3$, which was also observed in the SEM images (Fig. 1 (d)). The way in which the addition of Y_2O_3 affects the $BaTiO_3$ structure, is also reflected in the densification of the ceramics (Table 1). Even when in both cases (BT-A and BT-B) the densification decreases as the Y_2O_3 concentration increases, the ceramics issued from the BT-B powder present higher densification values. This is not surprising as one of the purposes of the added compounds to the $BaTiO_3$powder is to improve its densification.

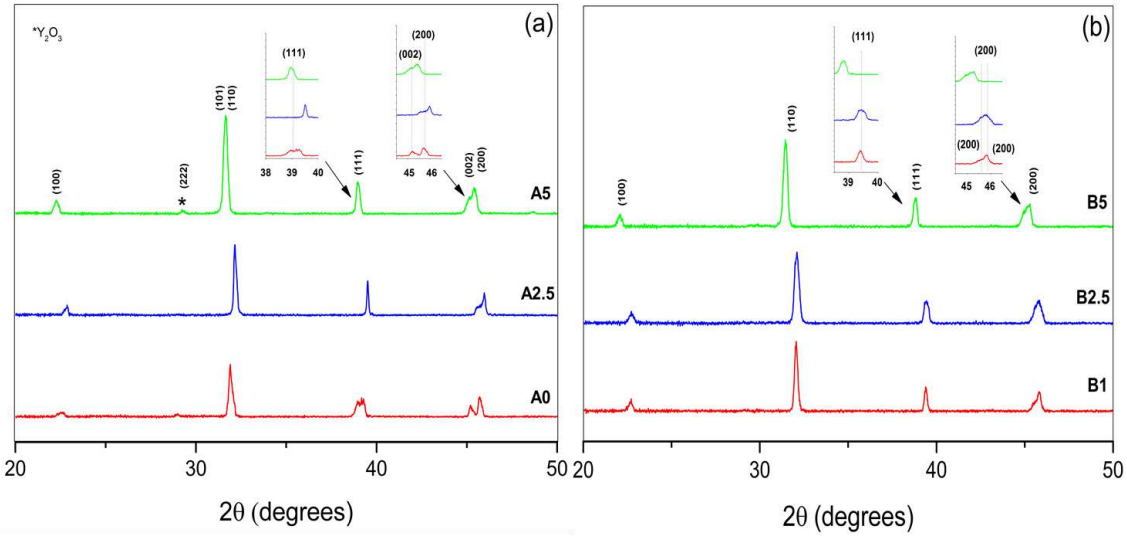

FIG. 3. X-ray diffraction patterns of undoped $BaTiO_3$ and Y_2O_3 - 2.5, 5.0 and 20 wt% - doped $BaTiO_3$ ceramics. Ceramics resulting from (a) BT-A and (b) BT-B.

IV. CONCLUSION

Pure and commercially formulated $BaTiO_3$ powder was doped with Y_2O_3 by traditional solid state reaction. The Y_2O_3 was added to pure $BaTiO_3$ and a commercial formulation that already contained 1 wt% of Y_2O_3, so that final concentrations were 2.5, 5 and 20 wt%. The samples, as powder and as ceramics, were analyzed by XRD. It was observed that as the Y_2O_3

concentration increases, the effects over the $BaTiO_3$ structure are more evident. The phase transition from tetragonal to a mixture of tetragonal and cubic was observed either in powder thermally treated as in the corresponding ceramics obtained from them. The results indicate that the additives in the commercial formulation have a strong interaction allowing a better densification and a change of phase more than in the powder and ceramics from pure $BaTiO_3$. It was even observed the formation of a secondary phase identified as $Ba_6Ti_{17}O_{40}$ in the Y_2O_3-doped (20 wt%) commercially formulated $BaTiO_3$ thermally treated powder. No secondary phases formed by $BaTiO_3$ and Y_2O_3 were found, free Y_2O_3 is evidence of surpassing its solubility limit. The changes in the lattice show that Y entered into the lattice, and induces the formation of a secondary phase without Y or other elements of the formulation. These tests were conducted in air, so the oxides were not reduced during the treatments.

ACKNOWLEDGEMENTS

The authors thank the financial support of the National Science and Technology Council of Mexico (CONACyT) and the Postgraduate Cooperation Program (PCP-RU2I), project 229286, between Mexico and France. We are also grateful with Kemet de México and Marion Technologies, France.

REFERENCES

[1] Y.Tsur, T. D., Dunbar, andC. A. Randall "Crystal and defect chemistry of rare earth cations in $BaTiO_3$," *J. Electroceram.*, vol. 7, no. 1, pp. 25-34,2001.

[2] M. J. Wang, H. Yang, Q. L. Zhang, L. Hu, D. Yu, Z. S. Lin, andZ. S. Zhang"Doping behaviors of yttrium, zinc and gallium in $BaTiO_3$ ceramics for AC capacitor application," *J. Mater. Sci. Mater. Electron.*, vol. 25, no. 7, pp. 2905-2912,2014.

[3] S. H. Yoon, Y. S. J. O. Park, Hong andD. S. Sinn"Effect of the pyrochlore ($Y_2Ti_2O_7$) phase on the resistance degradation in yttrium-doped $BaTiO_3$ ceramic capacitors," *J. Mater. Res.*, vol. 22, no. 9, pp. 2539-2543, 2007.

[4] T.Ashburn, and D. Skamser "Highly accelerated testing of capacitors for medical applications,"in Proceedings of the 5th SMTA Medical Electronics Symposium. California, USA, 2008, January.

[5] S. H.Yoon, S. H.Kang, S. H.Kwon, and K. H. Hur,"Resistance degradation behavior of Ca-doped $BaTiO_3$," *J. Mater. Res.*, vol. 25, no. 11, pp. 2135-2142, 2010.

[6] G. Liu, andR. D. Roseman "Effect of BaO and SiO_2 addition on PTCR $BaTiO_3$ ceramics,"*J. Mater. Sci.*,vol. 34, no. 18, pp. 4439-4445, 1999.

[7] K. E.Ösküz, M.Torman, S. Sen and U. Sen "Effect of sintering temperature on dielectric properties of SiO_2 Doped $BaTiO_3$ ceramics," *J. Int. Sci. Publ.: Mater. Methods Technol.*,vol. 10, pp. 361-366, 2016.

[8] J.Zhang, Y. Hou, M. Zheng, W. Jia, M. Zhu, and H. Yan "The occupation behavior of Y_2O_3 and its effect on the microstructure and electric properties in X7R dielectrics," *J. Am. Ceram. Soc.*, vol. 99, no. 4, pp. 1375-1382, 2016.

[9] M. J. Wang, H. Yang, Q. L. Zhang, Z. S. Lin, Z. S., Zhang, D. Yu, D. and L. Hu "Microstructure and dielectric properties of $BaTiO_3$ ceramic doped with yttrium, magnesium, gallium and silicon for AC capacitor application," *Mater. Res. Bull.*, vol. 60, pp. 485-491, 2014.

[10] C. H. Kim, K. J. Park, Y. J. Yoon, M. H. Hong, J. O. Hong and K. H. Hur"Role of yttrium and magnesium in the formation of core-shell structure of $BaTiO_3$ grains in MLCC," *J. Eur. Ceram. Soc.*, vol. 28, no. 6, pp. 1213-1219, 2008.

[11] K. J. Park, C. H. Kim, Y. J. Yoon, S. M. Song, Y. T. Kim, and K. H. Hur"Doping behaviors of dysprosium, yttrium and holmium in $BaTiO_3$ceramics," *J. Eur. Ceram. Soc*., vol. 29, no. 9, pp. 1735-1741, 2009.

[12] A. Belous, O. V'yunov, L. Kovalenko, and D. Makovec "Redox processes in highly yttrium-doped barium titanate," *J. Solid State Chem.*, vol. 178, no. 5, pp. 1367-1375, 2005.

[13] D. Makovec, Z. Samardžija, and M. Drofenik "Solid solubility of holmium, yttrium, and dysprosium in $BaTiO_3$," *J. Am. Ceram. Soc.*, vol. 87, no. 7, pp. 1324-1329, 2004.

[14] M. Paredes-Olguín, I. A. Lira-Hernández, C. Gómez-Yañez and F. P. Espino-Cortes "Compensation mechanisms at high temperature in Y-doped $BaTiO_3$,"*Physica B*, vol. 410, pp. 157-161, 2013.

[15] J. Zhi, A. Chen, Y. Zhi, P.M. Vilarinho andJ. L. Baptista "Incorporation of yttrium in barium titanate ceramics," *J. Am. Ceram. Soc.*, vol. 82, no. 5, pp. 1345-1348, 1999.

[16] O. I. V'yunov, L. Kovalenko, A. G. Belous and V. N. Belyakov "Oxidation of reduced Y-doped semiconducting barium titanate ceramics," *Inorg. Mater.*, vol. 41, no. 1, pp. 87-93, 2005.

[17] A. Belous, O. V'yunov, M. Glinchuk, V. Laguta, and D. Makovez "Redox processes at grain boundaries in barium titanate-based polycrystalline ferroelectrics semiconductors,"*J. Mater. Sci.*, vol. 43, no. 9, pp. 3320-3326, 2008.

[18] S. Senz, A. Graff, W. Blum, D. Hesse and H. P. Abicht "Orientation Relationships of Reactively Grown $Ba_6Ti_{17}O_{40}$ and $Ba_2TiSi_2O_8$ on $BaTiO_3$ (001) Determined by X-ray Diffractometry," *J. Am. Ceram. Soc.*, vol. 81, no. 5, pp. 1317-1321, 1998.

[19] G. Koschek, and E. Kubalek "On the Electronic Structure and the Local Distribution of the Second Phase $Ba_6Ti_{17}O_{40}$ in $BaTiO_3$ Ceramics," *Phys.Status Solidi A*, vol. 102, no. 1, pp. 417-424, 1987.

[20] S. J. Zheng, K. Du, X. H. Sang and X. L. Ma "TEM and STEM investigation of grain boundaries and secondphases in bariumtitanate," *Philos. Mag. A*, vol. 87, no. 34, pp. 5447-5459, 2007.

Determination of Radio Frequency Attenuation Signals of Ajilete FM (92.1MHz) and Compared with Existing Friis Formula, along Gambari-Oyo Road, Nigeria

Oyeleke, O[1]., Olatinwo, M.O[2]., and Sanni, M[3].

Physics Electronics, Science Technology Department, Federal Polytechnic, Offa, Kwara State, Nigeria.

Abstract— *This work measured experimentally, and calculated theoretically using the existing Friis Fomula, the Attenuation of 92.1 MHz (Ajilete FM) Signals along Gambari(Lat 8^o29^1N; Long 4^o29^1) – Oyo-Road(Lat 7^o50^1N; Long 3^o56^1E), Oyo State Nigeria. The two results were compared. The experimental Measurement campaign was achieved by using an appropriate design dipole antenna, well matched to (810 GSP Analyser), to determine the attenuation. The calculated results correlated very well with the measurements (Correlation Coefficient Value $R^2=1$). But, they are not accurate when compared with the measurements (Chi- square values equal zero for received power, measured attenuation). The inaccuracies of the results for the existing formula with the measurements may be due to hills, valleys, trees and bends along the links. Hence the accuracy of the model used can only be effectively confirmed in areas free of the obstacles mentioned above. By applying LEAST SQUARE fit method to the experimental measured data, the analytical models,* $P(x)= 0.0154x^2-1.3575x-38.7620$ and $A(x)= 0132x^2 -1.2464x-104.8487$, in the form of polynomial of degree two, *were obtained respectively for received power and measured attenuation. The analytical model obtained is therefore recommended for use in an area characterised with bends, valleys, hills and trees, since the model has taken into consideration all these factors. In addition, repeater stations should be installed for effective transmission and for wider coverage in forested and valley areas. Moreover, transmitter of higher value like ten kilowatts should be employed for long distance transmission.*

Keywords— Attenuation, Dipole, transmitter, model polynomial, Friis Fomula.

I. INTRODUCTION

Attenuation is the reduction in power density of electromagnetic waves as it propagates through space. This term is commonly used in wireless communication and signal propagation. Attenuations may be due to many effects such as free space loss, refraction, diffraction, reflection, aperture-medium, coupling loss and absorption. Attenuation is also influenced by terrain, contours, environments (urban or rural, vegetation and foliage), propagation medium, the distance between the transmitter and the receiver and height and location of antenna (Rhodes, 2001). The causes of attenuation are enumerated further.

However, the reflected waves may reduce or increase attenuation. Often it is possible to communicate beyond the normal LOS distance by exploiting the reflection from a tall building, nearby mountain, or water tower. If the top portion of a structure or hill can be seen readily by both transmitting and receiving antennas, it may be possible to achieve practical, communication by directing both antennas towards the point of maximum reflection. If the reflecting object is very large in term s of a wavelength, the path loss, including the reflection can be very low. If a structure or hill exists adjacent to an LOS path, reflected energy may either add to or subtract from the energy arriving from the direct path. If the reflected energy arrives at the receiving antenna with the same amplitude (strength) as the direct signal, but has the opposite phase, both sandals will cancel and communication will be impossible.

However, if the same conditions exist but both signals arrive in phase, they will add and double the signal strength. These two conditions represent destructive and constructive combinations of the reflected and direct waves. Reflection from the ground at the common midpoint between the receiving and transmitting antenna may also arrive as constructive or destructive manner. Generally, in the VHF 7 UHF range, the reflected wave is out of phase (destructive) with respect to the direct wave at vertical angles less than a few degrees above the horizon. Meanwhile, since the ground is not a perfect conductor, the amplitude of the reflected wave seldom approaches that of the direct wave. Thus, even though the two arrive out of phase, complete cancellation does not occur. Some improvement may result from using vertical polarization rather than horizontal polarization (Rhode, 2001)

Several models have been obtained by different researchers for predicting signal attenuations of radio signal by various attenuating factors. Some of these models do agree with the experimental measured values. This is evident in Sarat *et al.*, (2004) as the model used could not be used to determine the rain attenuation of Hassan town in Indian and another model

was necessary for the town. Barwick, *et al*., (2004) measured the attenuation of radio frequency through the situ-ice at scout-Amuden station. The measured power was compared with power expected in the absence of attenuation using Frii equation shown below

$$Pr/Pt = GtGr\lambda^2/16\pi^2d^2L \quad (1)$$

Where

P_r= the power received
P_t= the power input to the transmitter
G_t= the gain of the transmitter
G_r = the gain of the receiver
D= the distance from the transmitter to receiver
λ= the broadcast wavelength
L= the known system loss faction

The experimental results showed that attenuation length decreases as temperature decreases and it also confirmed that the attenuation length at radio frequencies is approximately larger than the attenuation length at optical frequencies (Barwick al., 2004)

The choice of the instrument used to measure the strength of radio signal among others is the type of the factor causing the attenuation. Barrel et al (2011), used a Horn Antenna due to the high reflectivity at the ice and sea surface at Moore Embayment, South of Minna Bluff to measure the in-situ average electric attenuation length for radio frequency signals broadcasted vertically the Rose-Ice Shelf Antarctica. After comparing the confirmed and the returned pulse, he ascribed the loss to be attenuation. He used the formula below to find the attenuation length of (75-1250) to be between 500 to 300m. In the cause of determining the best condition for radio communication, Shoewu and Edoko (2009) concluded that fog weather is better for radio communication compare to rain weather. The measured the radio frequency signals of Nigeria telecommunication at 7.2Ghz between Lagos (Latitude 6^o26^1N, longitude 3^o 27^1E) and distance of forty-eight kilometres, from Epe (Latitude 6^o32^1, Longitude 3^o52^1E).

The inaccuracy of these model is further confirmed Al-Basheir 2004) when he measured radio attenuation signal at (2.1 GHz) through a date palm trees in Abu Dhabi in Saudi Arabia. The measured results was were compared with existing model namely Exponential decay Model and maximum attenuation Model(EDM) , the model gives a poor fitting and which suggests that ITU-R model need to be re-visited.

Regression analysis can also be used to determine attenuation as Okumbor et al., (2014) used the method with Mat lab programme to characterise signal attenuation using pathloss exponent in South-South part of Nigeria to ascertain the rate of signal attenuation during dry season.

Cloud attenuation due to cloud liquid water content has been obtained from the radiosonde measurements using Salonel Model at a tropical location. The linear relationship was obtained between LWC and attenuation over the frequency range 10-100GHz give an estimate of cloud contribution to signal attenuation if cloud water content is known (Bijoy et al., 2014).

II. METHODOLOGY

The following procedures were taken in order to determine the attenuation values (measured) of 92.1 radio frequency signals along Ogbomosho/Gambari- oyo links

The attenuation was calculated using the Sanjaya and Jingsu formula of 2004 expressed as

$$A(dB)= 10\log_{10}[P_r/P_t] \quad \text{(Sanjaya and Jingsu, 2004)} \quad (2)$$

where:

A- The attenuation in decibel

P_{r-} =power received by a receiver at a particular distance

P_t- power transmitted from the station

For Ajilete FM, the transmission power is 2500W and the operating frequency is 92.1MHz.

The Friis formula was used to calculate the power received which were expressed as below

$$P_r(dBm) = P_t + G_t(dB) + G_r(dB) - FSL(dB) - A_t(dB) - A_r(dB) \quad (3)$$

(Sanjaya and Jingsu, 2004)

Where

P_r= power received

P_t= power transmitted

G_t= Transmitting antenna gain

G_r= receiving antenna gain

FSL= free space loss (path loss)

A_t= transmission line loss between transmitter and transmitting antenna

A_r = transmission line loss between receiver and receiving antenna

Where

$$FSL\ (dB) = 32.4 + 20\log d \quad (4)$$

Where f is measured in MHz and d in km

Substituting for FSL in equation (3) using equation (4)

$P_r(dB) = P_t(dBm) + G_t(dB) + G_r(dB) - (32.4 + 20\log f + 20\log d)$ where $A_t(dB)$&$A_r(dB)$ are negligible or equal zero.

$$P_r(dB) = P_t(dB) + G_t(dB) + G_r(dB) - 32.4 - 20\log f - 20\log d \quad (5)$$

Where 20 log d varies with distance

For the power received to be calculated, the power transmitted needs to be converted to dBm with the formula stated below

$$\text{Power transmitted } (P_t) \text{ in milliwat} = 10^{dB/10} \text{ (Sanjaya and Jingsu, 2004)} \quad (6)$$

$$dBm = 10\log P(mw) \quad (7)$$

$dBm = 10\log 2500000$

$=63.979dBm$

Where $20\log f = 39.28dB$

From equation 3

$Pr(dBm) = (63.979) + 9 + 1.5 - 32.4 - 39.285 - 20\log d$

Where $20\log d$ varies with distance

$$Pr(dBm) = 2.794 - 20\log d \quad (8)$$

Equation 8 was used to calculate the power received at regular interval of 2km and the values are recorded in table 1

Recall from equation (2)

$A(dB) = 10\log_{10}[Pr/Pt]$

Substitute for Pr in equation (2) using equation (8)

$$A = 10\log_{10}[2.794 - 20\log d/2500] \text{ since } P_t = 2500W \quad (9)$$

Equation 9 was used for attenuation calculation and the values obtained are shown in table 2

III. EXPERIMENTAL MEASURED VALUE OF ATTENUATION

To measure the attenuation, the half wave dipole was used because it is very useful as a mobile antenna and the car body can be used as conducting plane. The antenna was used to pick the being transmitted from 92.1MHz broadcasting station. The

antenna was connected to the analyser to determine the attenuation of the signal as the distance from the transmitting station increases. Lead accumulator cell was used to power the analyser to prevent interference, while the earpiece was used to monitor the audio signals transmitted.

To measure the attenuation, a designed and constructed dipole antenna was needed and to determine the length, the following parameters were taken into consideration, the wavelength (λ) the speed of light in vacuum (c) and frequency (f) are related by C=f λ, where c is the speed of light in vacuum, f is the frequency and λ is the wavelength. Since the radio station in concern is operating at frequency of 92.1MHz then, the wavelength of the signal is

$$\lambda = 3x10^{8}/92.1x10^{6} = 3.2572 \text{ m} \quad (10)$$

The length of the antenna constructed is λ /4=0.814m

The antenna constructed was attached to analyser and it was used to take measurement of power received in (dBm) from 92.1 MHz at regular interval of 2km.

The readings taken were in (dBm) shown in table 1. It was converted to milliwatt using equation 6 ($P_r=10^{dBm/10}$), and then to watt. The attenuation of the measured received power was determined using equation 2 expressed below as

$$A(dB) = 10\log_{10}[P_r/P_t].$$

IV. RESULTS AND DISCUSSION

The various readings taken are as shown in the tables below

TABLE 1
VARIATION OF DISTANCE WITH POWER RECEIVED AND POWER CALCULATED

Distance (KM)	Power Received(W)	Power Calculated(W)
2.0	$1x10^{-5}$	$4.758x10^{-4}$
4.0	$1.3183x10^{-7}$	$1.189x10^{-4}$
6.0	$1.2023x10^{-7}$	$5.286x10^{-5}$
8.0	$3.1623x10^{-10}$	$2.978x10^{-5}$
10.0	$1.0x\ 10^{-9}$	$1.903x10^{-5}$
12.0	$2.5119x10^{-10}$	1.321x10-5
14.0	$1.0233x10^{-9}$	$9.707x10^{-6}$
16.0	$1x10^{-9}$	$7.432x10^{-6}$
18.0	$6.3096x10^{-10}$	$5.872x10^{-6}$
20.0	$6.3096x10^{-10}$	$4.757x10^{-6}$
22.0	$6.3096x10^{-10}$	$3.937x10^{-6}$
24.0	6-3096x10^{-10}	$3.304x10^{-6}$
26.0	$6.3096x10^{-10}$	2.815x10-6
28.0	$3.9811x10^{-10}$	$2.427x10^{-6}$
30.0	$3.9811x10^{-10}$	$2.114x10^{-6}$
32.0	$2.5119x10^{-10}$	$1.858x10^{-6}$
34.0	$2.5119x10^{-10}$	$1.646x10^{-6}$
36.0	$1.4791x10^{-10}$	$1.468x10^{-6}$
38.0	$1.4791x10^{-10}$	$1.318x10^{-6}$
40.0	$1.4791x10^{-10}$	$1.189x10^{-6}$
42.0	$1.4791x10^{-10}$	$1.09x10^{-6}$
44.0	$2.5119x10^{-10}$	$9.829x10^{-7}$
46.0	$2.5119x10^{-10}$	$8.993x10^{-7}$
48.0	$1.5849x10^{-7}$	$8.259x10^{-7}$
50.0	$1.5849x10^{-7}$	$7.610x10^{-7}$
52.0	$1x10^{-10}$	$7.037x10^{-7}$
54.0	$1x10^{-10}$	$6.25x10^{-7}$
56.0	$1.4791x10^{-10}$	$6.067x10^{-7}$
58.0	$8.5114x10^{-10}$	$5.656x10^{-7}$
60.0	$1x10^{-10}$	$5.286x10^{-7}$
62.0	$1.0233x10^{-10}$	$4.950x10^{-7}$
64.0	$1.0233x10^{-10}$	4-645x10^{-7}

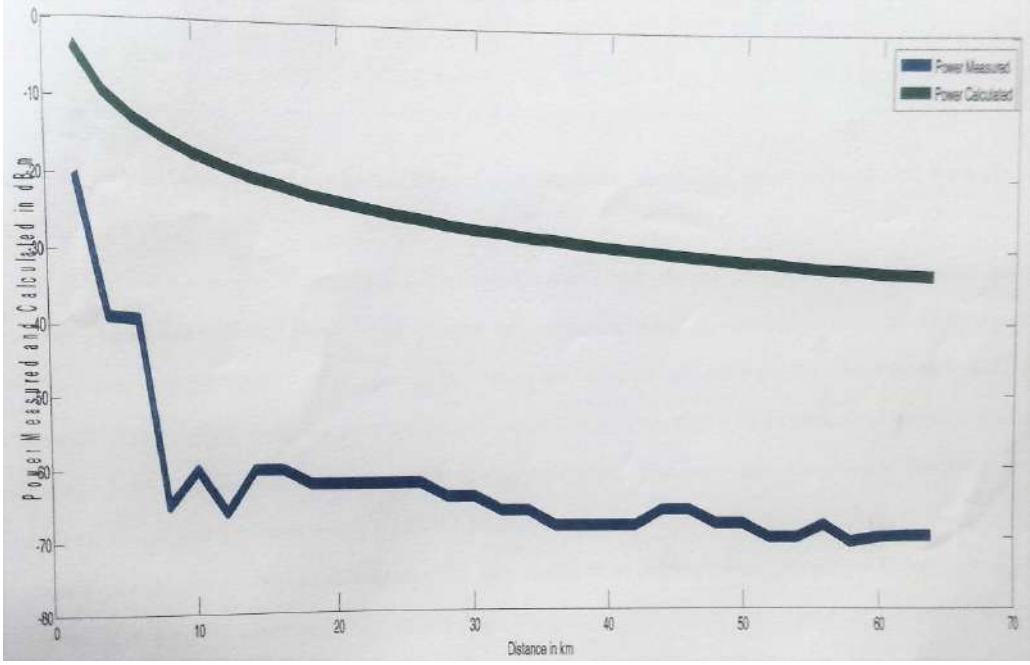

FIG 1: POWER MEASURED AND POWER RECEIVED AGAINST DISTANCE

TABLE 2
VARIATION OF DISTANCE WITH ATTENUATION MEASURED AND ATTENUATION CALCULATED

Distance (KM)	Attenuation Measured (dB)	Attenuation Calculated(dB)
2.0	-83.979	-67.205
4.0	-102.78	-73.227
6.0	-113.18	-76.748
8.0	-128.98	-79.24
10.0	-123.98	-81.185
12.0	-129.98	-82.77
14.0	-123.88	-84.109
16.0	-123.98	-85.268
18.0	-125.98	-86.292
20.0	-125.98	-87.206
22.0	-125.98	-88.034
24.0	-125.98	-88.789
26.0	-125.98	-89.484
28.0	-127.98	-90.129
30.0	-127.98	-90.728
32.0	-129.98	-91.289
34.0	-129.98	-91.815
36.0	-132.28	-92.312
38.0	-132.28	-92.78
40.0	-132.28	-93.228
42.0	-132.28	-93.605
44.0	-129.98	-94.054
46.0	-129.98	-94.44
48.0	-131.98	-94.81
50.0	-131.98	-95.165
52.0	-133.98	-95.506
54.0	-133.98	-95.834
56.0	-132.28	-96.149
58.0	-134.68	-96.454
60.0	-133.98	-96.748
62.0	-133.88	-97.033
64.0	-133.88	-97.31

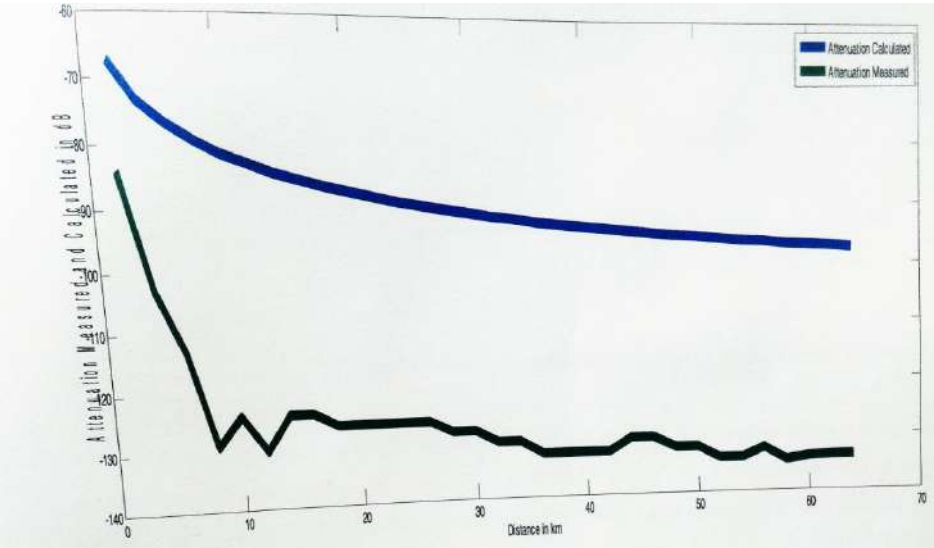

FIGURE 2: GRAPH OF ATTENUATION MEASURED AND ATTENUATION CALCULATED AGAINST DISTANCE

TABLE 3
STANDARD DEVIATION, CHI- SQUARE, PEARSON CORRELATION COMPARING POWER MEASURED AND POWER CALCULATED

	mean	Std. Deviation	N	Df	chi-square	Asymp. Sig	Peareson Correlation significant
Power Measured (dBm)	-62.7781	10.73895	32	13	14.375a	0.348	1
Power Calculated (dBm)	-25.3627	7.4334	32	31	.000b	1.666	0.881

TABLE 4
STANDARD DEVIATION, CHI- SQUARE, PEARSON CORRELATION AND STANDARD ERROR COMPARING MEASURED ATTENUATION AND CALCULATED ATTENUATION

	Mean	Std. Deviation	N	Df	Chi-Square	Asymp. Sig	Peareson Correlation significant
Power Measured (dBm)	-62.7781	10.73895	32	13	14.375a	0.348	1
Power Calculated (dBm)	-25.3627	7.4334	32	31	.000b	1.666	0.881

V. COMPARISON OF CALCULATED POWER (USING FRIIS FORMULA) AND MEASURED POWER RECIED RESULTS

There was a sharp deviation between calculated power received results and measured power received result when chi square test and standard deviation were calculated and the graph was plotted in which all these may be due to some factors not considered in the formula like, hills, valleys and forested areas. However, there is correlation between the two power because they are function of distance- as the distance increase from the transmitting station, the signal power continue to decrease

Using the method of least square fit, the analytical model was obtained from the graph of the received power(experimental measured data) in the form of polynomial equation of degree two

$P(x) = p_1x_n + p_2x^{n-1} + ----+p_nx+p_{n+1}$

$P(x) = 0.0154x^2-1.3575x-38.7620$

VI. COMPARISON OF CALCULATED AND EXPERIMENTAL VALUE OF ATTENUATION PLOTTED AGAINST DISTANCE

The attenuation against distance for the experimental values plotted is not a smooth curve in comparison with the experimental value. Also, there were deviations when chi square test, standard deviation and Pearson correlation coefficient

was calculated, the unsmooth curve and the deviation may be due to hills, valleys, trees and bends along the along the road. The standard mean square error of calculated attenuation was very high when compared with measured attenuation result.

The variation in the measured results and the calculated results which could be due to the above mentioned factor has revealed that the accuracy of friis model is subject to the availability of obstacles. This implies that the model would not be suitable for use

In an area that is characterised with hills, valley, trees and bends. Hence the obtained model, which takes into consideration the presence of the obstaches will always give a better result in experimental determination of attenuation.

The model obtained by Barrela et al (2011) was quiet difference from the model obtained in this work. This is understandable because the charatrics feature of that area was high reflectivity which is complexly deferent from the condition surrounding this research work.

Using the method of least square fit, the analytical model was obtained from the graph of attenuation measured (experimental measured data) in the form of polynomial of degree two

$P(x)= p_1x^n+p2x^{n-1}+----+ p_nx+p_{n+1}$

$A(x)= 0132x^2 -1.2464x-104.8487$

Comparison of calculated and experimental values of attenuation plotted against distance

VII. CONCLUSION AND RECOMMENDATION

7.1 Conclusion

The measured results were compared with the calculated results, using existing Friiis formula. The existing formula correlated very well with the measurement (R^2=1). But the existing model is not accurate when compared with the measurements, chi-square gives value of zero. The inaccuracy of the existing formula may be due to hill, valleys, trees and bends along the road. The obtained analytical models($A(x)= 0132x^2 -1.2464x-104.8487$ and $P(x)= 0.0154x^2-1.3575x-38.7620$) obtained for both power measured and attenuation measured are more reliable having taken into consideration the factors such as hill, bends, valleys , forest and trees which have limited the accuracy of the friis model.

7.2 Recommendations

To obtain reliable results of signal attenuation measurement in an area characterised with valleys, hills bends and forest, the models obtained in this work is recommended. Hence the Friis Model needs to be reviewed. A repeater station should be installed for effective transmission and for wider coverage in forested and valley areas. Moreover, transmitter of higher value like ten kilowatts should be employed for long distance transmission.

REFERENCES

[1] Al- Basheir, M.S., Shubair, R.M., and Shariff, S.M.(2006). Measurement and Analysis for Signal Attenuation through Date Palm Trees at 2.1 GHz Frequency. Sudan Engineering Society Journal, 52(45), pp. 17-22

[2] Barwick, S., Benson, D., Gorha, P. and Saltzberg. (2004). South Polar in SITU Radio Frequency Attenuation. Journal of Glaciology 32(180), pp. 1-27

[3] Barrilla, T., Barwick, S., and Saltzberg, D. (2011). Rose Ice Shelf(Antarctica) in SITU Radio Frequency Attenuation. Journal of Glaciology, 52(201), pp. 61-66

[4] Bijoy, K.M., and Debnath (2014). Attenuation of Signal at a Tropical Location with Radiosonde Data due to Cloud. International Journal of Smart Home 8(1) pp. 15-22

[5] Okumbor, N. Anthony and Okonkwo Obikwelu, Raphael(2014). Characterization of Signal Attenuation using Pathloss Exponent in South-South Nigeria. International Journal of Emerging Trends & Technology in Computer Science (IJETTCS) 3(3), pp.100-104

[6] Oyetunji, S. A., and Alowolodu, O. D. (2013). Determination of Propagation Path Loss and Contour Map for Adaba FM Radio Station in Akure N igeria. International Journal of Science and Technology 2 (9) pp. 661-668

[7] Sanjaya, G., and Jinghsu, Z. (2004). Attenuation of Microwaves Signal and its Impacts on Communication System. Department of Engineering, College of Engineering, University of North Texas, pp 1-10.

[8] Sarat, k.k., Vijaya, B.R.S., and Rao, D.N. (2008). Prediction of KU Band Rain Attenuation Using Data and Simulation for Hassan, India. International Journal of Computer and Network Security. 8(4.), pp. 10-15

[9] Shoewu, O, and Edeko, F.O. (2005). Microwave Signal Attenuation at GHz in Rain and Harmattan Weather. American Journal of Scientific and Industrial Research, 2(3), pp.332-345.

Kinetics of Ethyl Ester Production from Soybean and Sunflower Oils Catalyzed by Sodium Ethoxide

Telma Porcina Vilas Boas Dias[1], Betania Hoss Lunelli[2], Gisele A. Medeiros Hirata[3], Paulo Mielke Neto[4], Luis Alberto Follegatti-Romero[5], Eduardo Augusto Caldas Batista[6], Antonio José de Almeida Meirelles[7]

[1]Faculty of Biochemistry, Federal University of São João Del-Rei, 35501–296, Divinópolis, MG, Brazil.
[2]Pontifícia Universidade Católica de Campinas, Faculdade de Química, Campinas, São Paulo, Brazil.
[3]Department of Chemical Engineering, Federal University of Sao Paulo (UNIFESP), 09913-030 - Diadema/SP, Brazil.
[4,6,7]School of Food Engineering, University of Campinas – UNICAMP, 13083–862, Campinas, SP, Brazil.
[5]Department of Chemical Engineering, Polytechnic School, University of São Paulo, 05508-900, São Paulo, Brazil.

Abstract*—The present paper reports the kinetics of soybean and sunflower oils' ethanolysis. The transesterification reaction was carried out using a molar ratio of ethanol to oil of 9:1 and 1.0 wt% of sodium ethoxide as catalyst under stirring of 400 rpm. The reactions were performed in a stirred batch reactor at three different temperatures (308.15, 323.15 and 338.15 K) over a period of 120 min. The concentration of compounds was analyzed by High-Performance Size Exclusion Chromatography (HPSEC). The kinetic model assumed that ethanolysis occurs in a sequence of three reversible steps with the production of di- and monoacylglycerols as intermediate components. Based on the modeling approach it was possible to determine the rate constants of reaction and activation energies for the transesterification process of soybean and sunflower oils. Despite the phase splitting, no mass transfer control was observed and the proposed mathematical model fitted well the experimental data.*

Keywords: Ethanol, ethylic biodiesel, kinetics, soybean oil, sunflower oil.

I. INTRODUCTION

Biodiesel, a clean renewable fuel, is considered as the best candidate for a diesel fuel substitution because it can be used in any compression ignition engine without the need for modification [1]. Ethyl esters (ethyl biodiesel) are produced from triacylglycerols, which can react with ethanol in the presence of a catalyst, usually an alkali or acid catalyst, in a process known as transesterification. The transesterification reaction results in the production of three moles of ethyl esters (*EE*) and one mole of glycerol (*GL*) for each mole of triacylglycerol (*TG*), requiring three moles of alcohol. The reaction occurs as a sequence of three steps with intermediate formation of diacylglycerols (*DG*) and monoacylglycerols (*MG*) [2].

Most of the biodiesel produced in the world today is derived from soybean oil, however, all vegetable oils or triacylglycerols can be converted into biodiesel. Factors such as geography, climate and economics determine the vegetable oil of greater interest for potential use in biofuels. Thus, in the United States, for example, soybean oil is regarded as the main raw material and in some tropical countries, it is palm oil. The most common vegetable oils, whose raw materials are abundant in Brazil, are soybean, corn, peanuts, cotton, babassu and palm [3.4].

Methanol is most often used as alcohol in the biodiesel synthesis because of its suitable physical and chemical properties and low cost, but it is usually derived from fossil sources. The production of ethyl esters, rather than methyl esters, is of considerable interest because the ethyl ester based biodiesel is an entirely agricultural fuel [5,6].

Fatty acid esters are broadly available in nature and have been widely used as high–value fine chemicals in the food, cosmetic, pharmaceutical and rubber industries. Currently, fatty acid esters (biodiesel) are being considered as a promising substitute for conventional diesel fuels, due to environmental and economic problems related to the use of conventional fuels [7,10].

There are several variables, such as molar ratio of alcohol to vegetable oil, catalyst type, temperature, and presence of impurities, among others, that affect the transesterification process and should be investigated [11,12].

The transesterification kinetics for vegetable oils has been reported in a few studies. However, most of these studies do not take into account the formation of intermediate products, only the overall reaction, and consider the use of methanol instead of ethanol [13,16].

In this study, the kinetics of transesterification of soybean and sunflower oils with ethanol was investigated. The molar ratio of alcohol to oil, the catalyst concentration (sodium ethoxide) and the mixing intensity were kept constant while the temperature was varied. Kinetic data were collected at three temperature levels. The reaction rate constants and the activation energies were determined for all the forward and reverse reactions in the three temperature levels.

II. EXPERIMENTAL SECTION

Anhydrous ethanol and glacial acetic acid were purchased from Merck (Germany), with purity of 99.5 and 99.0 %, respectively. Tetrahydrofuran (THF) from Tedia, with purity of 99.8 %, and sodium ethoxide from Sigma Aldrich, with purity of 99 % were also used.

Refined soybean and sunflower oils were purchased in the local retail market (Bunge, Campinas/SP, Brazil).The fatty acid compositions of the vegetable oils studied in this work are presented in Table 1. These compositions were determined by gas chromatography of the fatty acid methyl esters using the official AOCS method (1–62) [17]. Prior to the chromatographic analysis the fatty compounds of the samples were converted into their respective fatty acid methyl esters using the method of Hartman and Lago[18]. The chromatographic analyses were carried out using a capillary gas chromatography system and the experimental conditions were obtained from Basso et al.[19].

TABLE 1
FATTY ACID COMPOSITIONS OF THE VEGETABLE OILS

Fatty acid	Symbol	Cx:y[a]	M[c] g.mol^{-1}	Soybean oil	Sunflower Oil
				100w[d]	
Dodecanoic	L	C12:0	200.32	0.00	0.06
Tetradecanoic	M	C14:0	228.38	0.05	0.02
Hexadecanoic	P	C16:0	256.43	10.72	6.30
cis-hexadec-9-enoic	Po	C16:1	254.42	0.07	0.09
Trans - hexadec-9-enoic		C16:1t[b]	254.42	0.00	0.03
Heptadecanoic	Ma	C17:0	270.45	0.06	0.03
cis-heptadec-9-enoic	Mg	C17:1	268.45	0.00	0.03
Octadecanoic	S	C18:0	284.49	2.80	3.31
cis-octadec-9-enoic	O	C18:1	282.47	25.94	35.98
cis,cis-octadeca-9,12-dienoic	Li	C18.2	280.45	53.00	52.75
trans,trans-octadeca-9,12-dienoic		C18:2t[b]	280.45	0.13	0.11
all-*cis*-octadeca-9,12,15-trienoic	Le	C18:3	278.44	6.34	0.78
Icosanoic	A	C20:0	312.54	0.31	0.30
cis–icos–9–enoic	Ga	C20:1	310.52	0.19	0.21
Docosanoic	Be	C22:0	340.59	0.39	0.00

[a]InCx:y, x = number of carbons and y = number of double bonds. [b] trans isomer. [c]M = molar mass. [d]w = mass fraction

Based on the fatty acid compositions, the possible compositions of triacylglycerol (Table 2) of the vegetable oils were calculated using the algorithm suggested by AntoniosiFilho et al.[20]. In order to calculate the probable triacylglycerol compositions, the quantities of *transisomers* (see Table 1) were computed with their respective *cis* isomers. In Table 2 the main triacylglycerol represents the component with the greatest composition in the isomer set with x carbons and y double bonds. Additionally, iodine values of vegetable oils were calculated from their fatty acid compositions according to the official method Cd 1c-85, recommended by AOCS [17]. These values are presented in Table 3 together with tabulated values extracted from Firestone[21] for soybean and sunflower oils. The iodine value reflects the degree of unsaturation of fatty compounds, so that the higher the iodine value the higher the degree of unsaturation.

TABLE 2
POSSIBLE TRIACYLGLYCEROL COMPOSITIONS OF SOYBEAN AND SUNFLOWEROILS.

Main *TG*[a]	Group x:y[b]	Molar mass (g.mol^{-1})	Soybean oil	Sunflower oil	Main *TG*[a]	Group x:y[b]	Molar mass (g.mol^{-1})	Soybean oil	Sunflower oil
			100w[c]					100w[c]	
POP	50:1	833.37	0.94	0.43	LiLiP	52:4	855.38	10.63	6.05
POS	52:1	861.42	0.44	0.48	SLnO	54:4	883.43	0.28	-
SOS	54:1	889.48	-	0.14	LiLiS	54:4	883.43	2.50	3.41
PLiP	50:2	831.35	1.93	0.63	OOLi	54:4	883.43	10.30	19.90
PLiS	52:2	859.41	0.91	0.71	LiLiA	56:4	911.48	0.25	0.24
OOP	52:2	859.41	2.50	2.77	LiLiBe	58:4	939.54	0.30	-
SLiS	54:2	887.46	0.11	0.20	PLiLn	52:5	853.36	2.56	-
OOS	54:2	887.46	0.59	1.56	SLiLn	54:5	881.41	0.61	-
OOA	56:2	915.51	-	0.10	OOLn	54:5	881.41	1.24	0.20
PLiBe	56:2	915.51	0.11	-	LiLiO	54:5	881.41	21.25	29.44
PLnP	50:3	829.34	0.23	-	LnLnP	52:6	851.34	0.15	-
PLnS	52:3	857.39	0.11	-	LiLiGa	56:5	909,47	-	0,11
PLiO	52:3	857.39	10.29	8.18	OLiLn	54:6	879.40	5.10	0.88
SLiO	54:3	885.44	2.42	4.61	LiLiLi	54:6	879.40	14.61	14.52
OOO	54:3	885.44	1.66	4.48	LnLnO	54:7	877.38	0.31	-
OLiA	56:3	913.50	0.24	0.32	LiLiLn	54:7	877.38	5.27	0.64
OLiBe	58:3	941.55	0.28	-	LnLnLi	54:8	875.37	0.64	-
PLnO	52:4	855.38	1.24	-					

[a]main TG in the group with x carbons and y double bounds. [b]In x:y, x = number of carbons (except for carbons of glycerol); y = number of double bonds. [c]w = mass fraction.

TABLE 3
IODINE VALUES AND AVERAGE MOLAR MASSES OF SOYBEAN AND SUNFLOWEROILS.

VegetableOil	IodineValue		Composition (100w[a])			Molar mass (g,mol^{-1})			
	Calculated	Literature [21]	*TG*	*DG*	*MG*	*TG*	*DG*	*MG*	Oil
Soybean	137.03	118-139	0.9574	0.0345	0.0081	886.46	622.09	357.77	873.06
Sunflower	130.49	118-145	0.9618	0.0263	0.0119	890.66	624.90	359.17	877.35

[a] w = mass fraction.

The ethanolysis of soybean and sun flower oils was carried out at 9:1 molar ratio of ethanol to oil and the sodium ethoxide amount of 1.00 % (based on the oil weight). The reaction was conducted at atmospheric pressure and temperatures of 308.15, 323.15 and 338.15 K. An agitation speed of 400 rpm was applied in all experiments.

Glass equilibrium cells, such as those described by Silva et al.[22], were used for the experiments. The Vegetable oil (100.00 g) was stirred at the desired temperature for about 30 min. Ethanol and sodium ethoxide were kept at the desired temperature and then added to the system. Each component was weighted on an analytical balance (Precisa, model XT220A, Sweden), accurate to (0.0001 g). The agitation was maintained with a magnetic stirrer (IkaWerke, model RH-KT/C, Staufen, Germany), and the temperature was controlled with a thermostatic bath (Cole Parmer model 12101-55, Chicago, U.S.A.) accurate to (0.01 K). During the reaction samples (0.5 ml) were taken from the reaction mixture, and immediately dissolved in 25 ml of THF and filtered through a 0.45 μm Millipore filter. All samples were analyzed by High Pressure Size Exclusion Chromatography (HPSEC).

The composition of the samples, in terms of triacylglycerols (*TG*), diacylglycerols (*DG*), monoacylglycerols (*MG*), ethyl esters (*EE*), ethanol (*ET)* and glycerol (*GL*), was determined by HPSEC. The methodology was adapted from Schoenfelder[23], however the columns proposed by this method were replaced by three Phenogel columns 50A, 100 A and 500 A, (300 mm x 7.8 mm).

The quantification was carried out on a Shimadzu VP series HPLC equipped with two LC–10ADVP solvent delivery units for binary gradient elution, a model RID10A differential refractometer, an automatic injector with an injection volume of 20

μL, a model CTO−10ASVP column oven for precision temperature control even at sub−ambient temperatures, a model SCL–10AVP system controller and LC–Solution 2.1 software for remote management.

The results obtained in the chromatograms were converted to molar concentrations of each component based on calibration curves expressed in mass concentration ($g.L^{-1}$). The molar concentrations $[C_i]$($mol.L^{-1}$) were calculated from the mass concentrations using molar mass of the components or the average molar mass of the class of components.

The same analytical procedure described above was used for evaluating the refined oils composition in terms of *TG*, *DG* and *MG*. Based on these results and on the probable triacylglycerol compositions (Table 2), the average molar masses of *TG*, *DG* and *MG* fractions of the vegetable oils were calculated. These calculations were performed considering the stoichiometry relating the *TG* fraction to the *DG* and *MG* fractions. The oil composition in terms of *TG*, *DG* and *MG* and the corresponding average molar masses are given in Table 3.

The oil conversion degree, X (in %), was calculated from the content of acylglycerols in the mixture at the beginning and the end of the reaction process by the following (1):

$$X = \frac{(w_{TG0} + w_{DG0} + w_{MG0}) - (w_{TG} + w_{DG} + w_{TG})}{(w_{TG0} + w_{DG0} + w_{MG0})}.100$$

Where w_{TGO}, w_{DGO} and w_{MGO} are the mass fractions of *TG*, *DG* and *MG* at the initial reaction time, respectively, and w_{TG}, w_{DG} and w_{MG} are the corresponding fractions at the final time.

The kinetic model assumed for the transesterification process has been fitted with the aid of a program written in FORTRAN software. The integration of the model ordinary differential equations was performed using the Runge-Kutta 4th order method. To estimate the kinetic parameters, an optimization technique based on genetic algorithm (GA) was used [24]. The optimizer algorithm developed by Carroll [25] was adapted, as indicated in prior works reported in the literature [26, 27], for minimizing the differences between the kinetic model predictions and the experimental data, using the following objective function (2):

$$F_{OBJ} = \sum_{i=1}^{I}\sum_{k=1}^{K}\left(\frac{C_{sim\,i,k} - C_{\exp\,i,k}}{C_{exp_{max}}}\right)^2$$

With$i$ varying over time and C_k referring to the molar concentrations of the reaction components or class of components (TG, DG, MG).

The kinetic model was based on the approach proposed by Noureddini & Zhu [16], in which the following reactions are considered (3):

$$TG + ET \underset{k_2}{\overset{k_1}{\rightleftharpoons}} DG + EE$$

$$DG + ET \underset{k_4}{\overset{k_3}{\rightleftharpoons}} MG + EE$$

$$MG + ET \underset{k_6}{\overset{k_5}{\rightleftharpoons}} GL + EE$$

The set of differential equations characterizing the stepwise reaction for oil transesterification is shown below (4), (5), (6), (7), (8), and (9):

$$\frac{d[C_{TG}]}{dt} = -k_1[C_{TG}][C_{ET}] + k_2[C_{DG}][C_{ET}]$$

$$\frac{d[C_{DG}]}{dt} = k_1[C_{TG}][C_{ET}] - k_2[C_{DG}][C_{EE}] - k_3[C_{DG}][C_{ET}] + k_4[C_{MG}][C_{EE}]$$

$$\frac{d[C_{MG}]}{dt} = k_3[C_{DG}][C_{ET}] - k_4[C_{MG}][C_{EE}] - k_5[C_{MG}][C_{ET}] + k_6[C_{GL}][C_{EE}]$$

$$\frac{d[C_{EE}]}{dt} = k_1[C_{TG}][C_{ET}] - k_2[C_{DG}][C_{EE}] + k_3[C_{DG}][C_{ET}] - k_4[C_{MG}][C_{EE}] + k_5[C_{MG}][C_{ET}] - k_6[C_{GL}][C_{EE}]$$

$$\frac{d[C_{GL}]}{dt} = k_5[C_{MG}][C_{ET}] - k_6[C_{GL}][C_{EE}]$$

$$\frac{d[C_{ET}]}{dt} = -\frac{d[C_{EE}]}{dt}$$

Where k_1 to k_6 are reaction rate constants; *TG, DG, MG, GL, ET*, and *EE* are the concentrations of the components in the reaction mixture. Note that the rate constants associated with the overall reaction were not considered since, as indicated by Noureddini & Zhu [16], their effects are negligible.

The initial values of the kinetic constants of reaction (k_i) were estimated by linear regression of the concentrations of reactants and products over time obtained experimentally and subsequently adjusted using the genetic algorithm optimization method. Having the values of the kinetic constants (k_i), the activation energies (E_a) and pre-exponential factors(A) were determined by linearization of the Arrhenius(10).

$$ln(k) = -\left(\frac{E_a}{R}\right) \times \frac{1}{T} + ln(A)$$

Where A is the pre-exponential factor, E_a is the activation energy, and R is the gas constant.

III. RESULTS AND DISCUSSION

Typical concentration curves for the transesterification of soybean oil at 308.15 K and sunflower oil at 338.15 K are presented in Fig. 1 and 2, respectively. These figures show the rate of consumption of triacylglycerol's and formation of ethyl esters and glycerol as well as of the intermediate compounds.

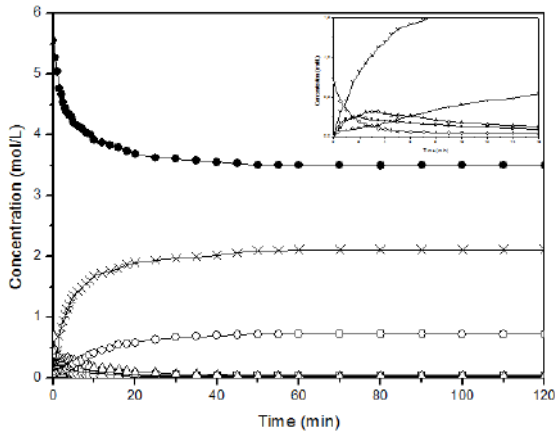

FIG. 1 –THE COMPOSITION OF THE REACTION MIXTURE DURING THE TRANSESTERIFICATION OF SOYBEAN OIL AT 308.15 K. EXPERIMENTAL DATA: (–◊–) TRIACYLGLYCEROL; (–□–) DIACYLGLYCEROL; (–Δ–) MONOACYLGLYCEROL; (–×–) ETHYL ESTER; (–○–) GLYCEROL AND (–●–) ETHANOL.

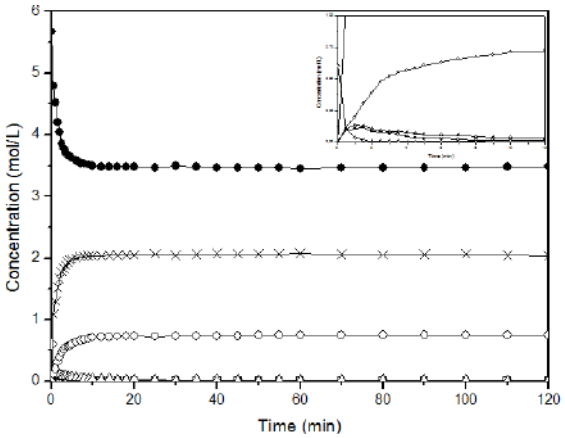

FIG. 2 – THE COMPOSITION OF THE REACTION MIXTURE DURING THE TRANSESTERIFICATION OF SUNFLOWER OIL AT 338.15 K. EXPERIMENTAL DATA: : (–◊–) TRIACYLGLYCEROL; (–□–) DIACYLGLYCEROL; (–Δ–) MONOACYLGLYCEROL; (–×–) ETHYL ESTER; (–○–) GLYCEROL AND (–●–) ETHANOL.

The first stage of the transesterification of triacylglycerols may be controlled by mass transfer. Due to the fact that the oil is not fully miscible with alcohol, this stage might be characterized by slow reaction rates, hence the importance of a good stirring at this stage in order to avoid any mass transfer constraint. In general, the first step is faster when the reaction is ethanolysis, instead of the methanolysis, due to the difference in the oil solubility in both. The second stepis rapidand is controlled byreaction kinetics, while the latter is dominated by the reaction chemical equilibrium [28,29].

The production rate of ethyl esters in Fig. 1 and 2 starts with a sudden increase followed by a lower production rate when the reaction approaches equilibrium. Darnako and Cheryan [14] and Noureddine and Zhu [16] have observed a sigmoidal pattern for production of methyl esters. This pattern consists of a slow rate at the beginning, followed by a sudden surge and finally a slow rate again, especially at low temperatures. These authors explained that the initial mass transfer-controlled region could be eliminated if sufficient mixing is provided.

Fig. 1 and 2 show that no period controlled by mass transfer occurs in the present study, being the reaction path controlled only by its kinetics. Ahiekpor and Kuwornoo [13] also observed the same behavior in the study of palm oil ethanolysis.

The assays were performed at three different temperatures (308.15, 323.15, and 338.15 K) and the kinetic rate constants were estimated for these temperatures. The calculated values are shown in Table 4. Fig. 3 and 4 show the concentration profiles of experimental and simulated data for the transesterification process of soybean and sunflower oils, respectively, at 323.15 K.

TABLE 4
THE RATE CONSTANTS AT DIFFERENT TEMPERATURES

Rate constants ($L.mol^{-1}.min^{-1}$)						
Temperature (K)	k_1	k_2	k_3	k_4	k_5	k_6
Soybean oil						
308.15	0.1019	0.0236	0.1254	0.2554	0.0578	0.0042
323.15	0.2720	0.0593	0.3586	0.2671	0.0525	0.0125
338.15	0.3312	0.0615	0.4374	0.2844	0.0927	0.0128
Sunflower oil						
308.15	0.1067	0.0286	0.1334	0.2533	0.0464	0.0078
323.15	0.2381	0.0674	0.4693	0.9456	0.1287	0.0197
338.15	0.3483	0.1414	0.9286	1.0942	0.2498	0.0230

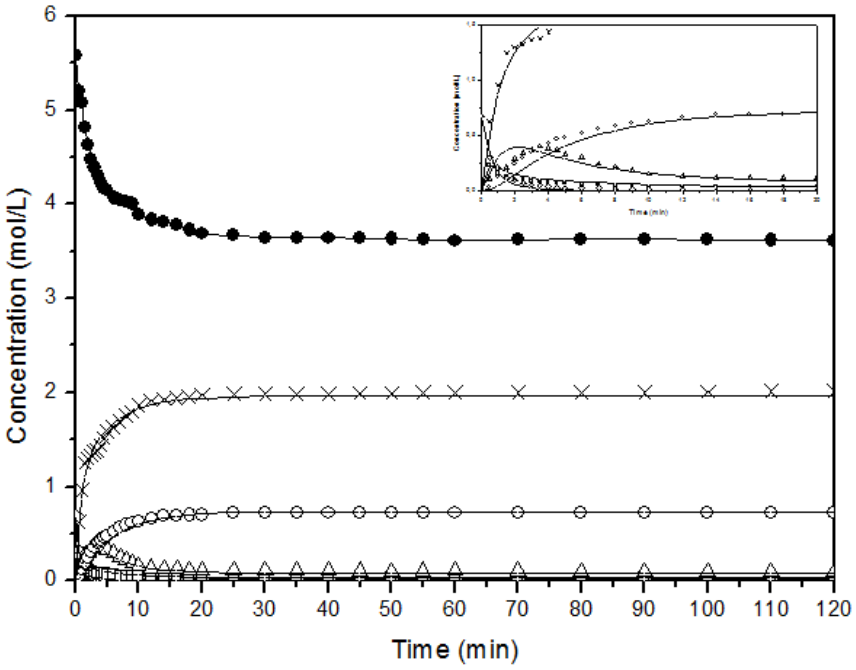

FIG. 3 –THE COMPOSITION OF THE REACTION MIXTURE DURING THE TRANSESTERIFICATION OF SOYBEAN OIL AT 323.15 K. (——) SIMULATION RESULTS AND EXPERIMENTAL DATA : (◊) TRIACYLGLYCEROL; (□) DIACYLGLYCEROL; (Δ) MONOACYLGLYCEROL; (×) ETHYL ESTER; (○) GLYCEROL AND (●) ETHANOL.

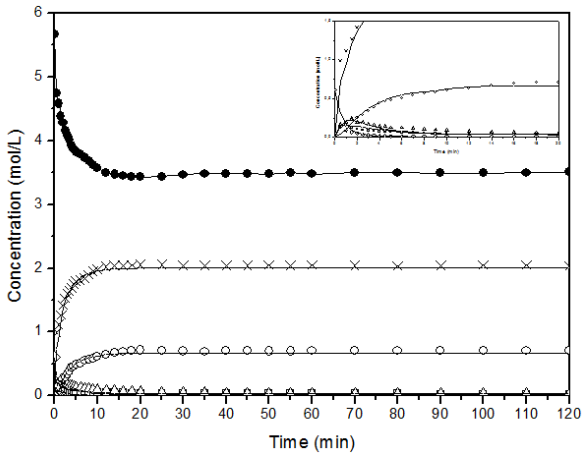

FIG. 4 – THE COMPOSITION OF THE REACTION MIXTURE DURING THE TRANSESTERIFICATION OF SUNFLOWER OIL AT 323.15 K. (——) SIMULATION RESULTS AND EXPERIMENTAL DATA (◊) TRIACYLGLYCEROL; (□) DIACYLGLYCEROL; (Δ) MONOACYLGLYCEROL; (×) ETHYL ESTER; (○) GLYCEROL AND (●) ETHANOL.

The dependence of the overall conversion in relation to the temperature is presented in Fig. 5 (A) and (B) for soybean and sunflower oils, respectively. In accordance with these Figures, the tests conducted at higher temperatures resulted in faster and higher conversion rates. These Figures also show that, over the temperature range of 308.15-323.15 K, approximately forty minutes of reaction time are sufficient to achieve maximum oil conversion to ethyl esters. We can also observe that for the temperature of 338.15K the maximum conversion was already achieved after approximately twenty minutes.

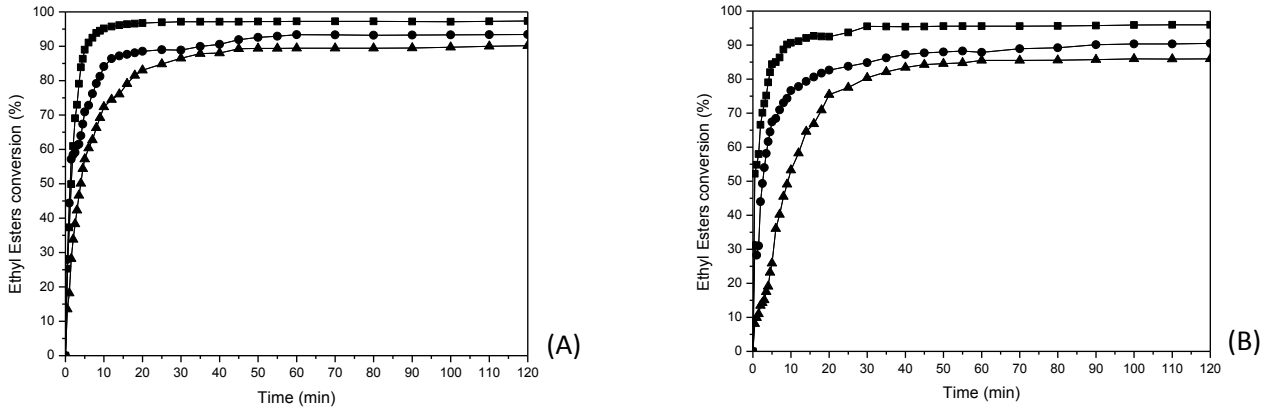

FIG. 5 – THE EFFECT OF THE TEMPERATURE AND TIME ON THE OVERALL CONVERSION TO ETHYL ESTERS FOR SOYBEAN OIL (A) AND SUNFLOWER OIL (B). (▲) 308.15 K; (●) 323.15 K; (■) 338.15 K.

The Arrhenius (6) was applied for determining the activation energies and pre-exponential factors for the ethanolysis reactions of soybean and sunflower oils, respectively, and the values obtained are shown in Table 5.

TABLE 5
ACTIVATION ENERGIES AND PRE-EXPONENTIAL FACTORS FOR THE REACTION STEPS OF ETHANOLYSIS OF SOYBEAN AND SUNFLOWER OILS.

Reaction	Soybean oil		Sunflower oil	
	Activation energy ($cal.mol^{-1}$)	Pre-exponential factor ($L.mol^{-1}.min^{-1}$)	Activation energy ($cal.mol^{-1}$)	Pre-exponential factor ($L.mol^{-1}.min^{-1}$)
$TG \rightarrow DG$	8203.426	$7.59x10^{4}$	8197.167	7.42×10^{4}
$DG \rightarrow TG$	6698.938	$1.53x10^{3}$	11023.56	1.91×10^{6}
$DG \rightarrow MG$	8702.558	$2.13x10^{5}$	13429.72	4.89×10^{8}
$MG \rightarrow DG$	739.559	$8.52x10^{-1}$	10206.87	5.28×10^{6}
$MG \rightarrow GL$	3183.908	9.42	11637.45	8.79×10^{6}
$GL \rightarrow MG$	7791.455	$1.67x10^{3}$	7498.372	1.84×10^{3}

As it can be seen, for soybean oil the first two reactions (TG↔DG and DG↔MG) are favored by high temperatures. However, for the third step (MG↔GL) the forward reaction has lower activation energy than the reverse reaction, indicating a more favorable reverse reaction at higher temperatures. This same behavior was observed by Noureddini & Zhu [16], although the calculated activation energies for the three-step reactions in the present case are slightly lower than the corresponding values obtained by these authors for the methanolysis of soybean oil.

In case of sunflower oil the observed behavior is different, since the last two reactions (DG↔MG and MG↔GL) are favored by high temperatures. On the other hand, in the first step (TG↔MG) the forward reaction has lower activation energy than the reverse reaction, indicating a more favorable reverse reaction at higher temperatures. Values obtained in the present work are within an acceptable range according to data reported in the literature[30,31].

IV. CONCLUSION

The experimental data of concentration versus time showed that the production rate of ethyl esters started with a sudden surge followed by a lower production rate when the reaction approaches equilibrium, and the concentration profiles did not followed the sigmoidal behavior observed in the methanolysis.

The reaction rate constants, the corresponding activation energies, and pre-exponential factors reproduced very satisfactorily the process studied, showing that the developed kinetic model can be used to describe the ethanolysis process of soybean and sunflower oils adequately.

ACKNOWLEDGEMENTS

The authors acknowledge FAPEMIG (Fundação de Amparo à Pesquisa do Estado de Minas Gerais), CNPq (Conselho Nacional de Desenvolvimento Científico e Tecnológico, 483340/2012–0, 501926/2013-5, 406856/2013-3 and 305870/2014-9) and FAPESP (Fundação de Amparo à Pesquisa do Estado de São Paulo, 2008/56258–8) for the financial support.

REFERENCES

[1] Xu, G.; Wu, G.-y., The investigation of blending properties of biodiesel and No. 0 diesel fuel. *Journal Jiangsu Ploytechnic Univers*, 15, 8-16, 2003.

[2] Ma, F. R.; Hanna, M. A., Biodiesel production: a review. *Bioresource Technology*, 70, (1), 1-15, 1999.

[3] Barnwal, B. K.; Sharma, M. P., Prospects of biodiesel production from vegetable oils in India. *Renewable and Sustainable Energy Reviews*, 9, (4), 363-378, 2005.

[4] Pousa, G. P. A. G.; Santos, A. L. F.; Suarez, P. A. Z., History and policy of biodiesel in Brazil. *Energy Polic*, 35, (11), 5393-5398, 2007

[5] Clark, S. J.; Wagner, L.; Schrock, M. D.; Piennaar, P. G., Methyl and ethyl soybean esters as renewable fuels for diesel engines. *Journal of the American Oil Chemists Society*,61, (10), 1632-1638, 1984

[6] Encinar, J. M.; González, J. F.; Rodríguez, J. J.; Tejedor, A., Biodiesel Fuels from Vegetable Oils: Transesterification of Cynara cardunculus L. Oils with Ethanol. *Energy & Fuel*, 16, (2), 443-450, 2002.

[7] Keng, P. S.; Basri, M.; Zakaria, M. R. S.; Rahman, M. B. A.; Ariff, A. B.; Rahman, R. N. Z. A.; Salleh, A. B., Newly synthesized palm esters for cosmetics industry. *Industrial Crops and Products*, 29, (1), 37-44, 2009.

[8] Kim, J.; Altreuter, D.; Clark, D.; Dordick, J., Rapid synthesis of fatty acid esters for use as potential food flavors. *J Amer Oil Chem Soc*, 75, (12), 1109-1113, 1998.

[9] Pérez-Feás, C.; Barciela-Alonso, M.; Sedes-Díaz, A.; Bermejo-Barrera, P., Phthalates determination in pharmaceutical formulae used in parenteral nutrition by LC-ES-MS: importance in public health. *Anal Bioanal Chem*, 397, (2), 529-535, 2010.

[10] Vermeulen, R.; Jönsson, B. G.; Lindh, C.; Kromhout, H., Biological monitoring of carbon disulphide and phthalate exposure in the contemporary rubber industry. *Int Arch Occup Environ Health*, 78, (8), 663-669, 2005.

[11] Freedman, B.; Pryde, E. H.; Mounts, T. L., Variables affecting the yields of fatty esters from transesterified vegetable oils. *Journal of the American Oil Chemists Society*, 61, (10), 1638-1643, 1984.

[12] Sankaran, V., Transesterification of Triglycerides. *United State. Patent*, 4, 866-876, 1990.

[13] Ahiekpor, J. C.; Kuwornoo, D. K., Kinetics of palm kernel oil and ethanol transesterification. *International Journal of Energy and Environment*,1, 1097-1108, 2010.

[14] Darnoko, D.; Cheryan, M., Kinetics of palm oil transesterification in a batch reactor. *Journal of the American Oil Chemists Society*,77, (12), 1263-1267, 2000.

[15] Marjanović, A. V.; Stamenković, O. S.; Todorović, Z. B.; Lazić, M. L.; Veljković, V. B., Kinetics of the base-catalyzed sunflower oil ethanolysis. *Fuel*, 89, (3), 665-671, 2010.

[16] Noureddini, H.; Zhu, D., Kinetics of transesterification of soybean oil. *Journal of the American Oil Chemists Society*, 74, (11), 1457-1463, 1997.

[17] AOCS, Official Methods and Recommended Practices of the American Oil Chemists' Society. *AOCS Press: Champaign, IL* **1998,** 5th ed.

[18] Hartman, L.; Lago, R. C. A., Rapid Preparation of Fatty Acid Methyl Esters From Lipids. *Laboratory Practice, London,* 22, 475-476, 1973.

[19] Basso, R. C.; de Almeida Meirelles, A. J.; Batista, E. A. C., Liquid–liquid equilibrium of pseudoternary systems containing glycerol + ethanol + ethylic biodiesel from crambe oil (Crambe abyssinica) at T/K = (298.2, 318.2, 338.2) and thermodynamic modeling. *Fluid Phase Equilibria,* 333, (0), 55-62, 2012.

[20] Filho, N. R. A.; Mendes, O. L.; Lanças, F. M., Computer prediction of triacylglycerol composition of vegetable oils by HRGC. *Chromatographia,* 40, (9-10), 557-562, 1995.

[21] Firestone, D., *Physical and Chemical Characteristics of Oils, Fats and Waxes*. p 151, 1999.

[22] Silva, L. H. M. d.; Coimbra, J. S. R.; Meirelles, A. J. d. A., Equilibrium Phase Behavior of Poly(ethylene glycol) + Potassium Phosphate + Water Two-Phase Systems at Various pH and Temperatures. *Journal of Chemical & Engineering Data,* 42, (2), 398-401, 1997.

[23] Schoenfelder, W., Determination of monoglycerides, diglycerides, triglycerides and glycerol in fats by means of gel permeation chromatography [C-VI 5b(02)]. *European Journal of Lipid Science and Technology,* 105, (1), 45-48, 2003.

[24] Holland, J. H., *Adaptation in Natural and Artificial Systems: An Introductory Analysis with Applications to Biology, Control and Artificial Intelligence*. MIT Press, p 228, 1992.

[25] Carroll, D. L., Chemical laser modeling with genetic algorithms. *AIAA Journal,* 34, (2), 338-346, 1996.

[26] Lunelli, B. H.; Melo, D. N. C.; Morais, E. R. d.; Victorino, I. R. S.; Toledo, E. C. V. d.; Maciel, M. R. W.; Filho, R. M., Real-time optimization for lactic acid production from sucrose fermentation by Lactobacillus plantarum. *21st European Symposium on Computer Aided Process Engineering,* 1396-1400, 2001.

[27] Victorino, I. R. d. S., *Optimization of an industrial reactor of cyclic alcohol production using genetic algorithms*. PhD Thesis (in Portuguese). School of Chemecal Engineering, UNICAMP, Campinas/SP, 2005.

[28] Zhou, W.; Boocock, D. G. B., Phase distributions of alcohol, glycerol, and catalyst in the transesterification of soybean oil. *J Amer Oil Chem Soc,* 83, (12), 1047-1052, 2006.

[29] Zhou, W.; Boocock, D. G. B., Phase behavior of the base-catalyzed transesterification of soybean oil. *J Amer Oil Chem Soc,* 83, (12), 1041-1045, 2006.

[30] Bambase, M. E., Jr.; Nakamura, N.; Tanaka, J.; Matsumura, M., Kinetics of hydroxide-catalyzed methanolysis of crude sunflower oil for the production of fuel-grade methyl esters. *Journal of Chemical Technology and Biotechnology,* 82, (3), 273-280, 2007.

[31] Vicente, G.; Martinez, M.; Aracil, J.; Esteban, A., Kinetics of sunflower oil methanolysis. *Industrial & Engineering Chemistry Research,* 44, (15), 5447-5454, 2005.

Effect of different sulfur content in Natural Rubber mixtures on their thermo-mechanical and surface properties

Kinga Tamási[1], Mariann Szabóné Kollár[2]

Department of Ceramic and Polymer Engineering, University of Miskolc, Hungary

Abstract*— *In this study, a field experiment was conducted to find out the effect of different levels of sulfur on natural rubbers mixtures. Vulcanization is a chemical process for converting natural rubber or related polymers into more durable materials by heating them with sulfur other equivalent curatives with accelerators. These additives modify the polymer by forming cross-links (bridges) between individual polymer chains. Vulcanized materials are less sticky and have superior mechanical properties. The results indicated that the application of sulfur -as a vulcanasing agent-had significant effect on mechanical (Shore A hardness test), thermal (DSC calorimetry) and surface-optical properties (SEM microscopy) of mixtures.

Keywords*— *vulcanization, sulfur, natural rubber, additives, cross-links.

I. INTRODUCTION

By far the most common vulcanizing methods depend on sulfur. Sulfur, by itself, is a slow vulcanizing agent and does not vulcanize synthetic polyolefins. Even with natural rubber, large amounts of sulfur, as well as high temperatures and long heating periods are necessary and one obtains to an unsatisfactory crosslinking efficiency with unsatisfactory strength and aging properties. Only with vulcanization accelerators can the quality corresponding to today's level of technology be achieved. The multiplicity of vulcanization effects demanded cannot be achieved with one universal substance; a large number of diverse additives, comprising the "cure package," are necessary. The combined cure package in a typical rubber compound consists of sulfur together with an assortment of compounds that modify the kinetics of crosslinking and stabilize the final product. In this study the following sulfur quantities were used per samples: S_1=3,80 g; S_2=7,6 g; S_3=11,40 g; S_4=15,20 g; S_5=19 g at pressure 220 bar and temperature 145°C and t=10 minutes.

II. THEORETICAL APPROACH OF VULCANISATION WITH SULFUR

Vulcanization is a chemical process that converts natural rubber elastomers into cross-linked polymers. The most common vulcanization agent is sulfur. It forms bridges between individual polymer molecules when heated with rubber. Often a catalyst and initiator is added to accelerate the vulcanization process. The cross-linked elastomers have much improved mechanical properties. In fact, unvulcanized rubber has poor mechanical properties and is not very durable.

The cross-linking process is rather complicated and involves a sequence of reactions. A free-radical mechanisms was originally assumed which has been described in great detail by Paul J. Flory (1953) and others [1]. However, all evidence points to an ionic mechanism because neither radicals could be detected nor do free-radical inhibitors and retarders effect sulfur vulcanization whereas organic acids, bases as well as solvents of high dielectric constant accelerate sulfur cure [2]. A possible reaction mechanism for polyisoprene (natural rubber) is shown below. The process starts with the formation of a persulfonium ion (I) by reaction of an isoprene unit with a polarized sulfur molecule or with a sulfur cation. The persulfonium ion reacts than with another isoprene unit by allylic hydrogen abstraction to produce a polymeric allylic carbocation (II). In a third step a sulfur molecule (cyclic S8) combines with the allylic cation to produce another sulfonium ion (IV) which releases (monomeric) sulfur. The polymeric sulfonium ion then undergoes crosslinking by anionic addition to a polymeric double bond to create a new carbocation (V) which then either reacts with another sulfur molecule or it abstracts hydrogen from another isoprene unit to create a new polymeric cation (II).

In a third step a sulfur molecule (cyclic S8) combines with the allylic cation to produce another sulfonium ion (IV) which releases (monomeric) sulfur. The polymeric sulfonium ion then undergoes crosslinking by anionic addition to a polymeric double bond to create a new carbocation (V) which then either reacts with another sulfur molecule or it abstracts a hydrogen from another isoprene unit to create a new polymeric cation (II).

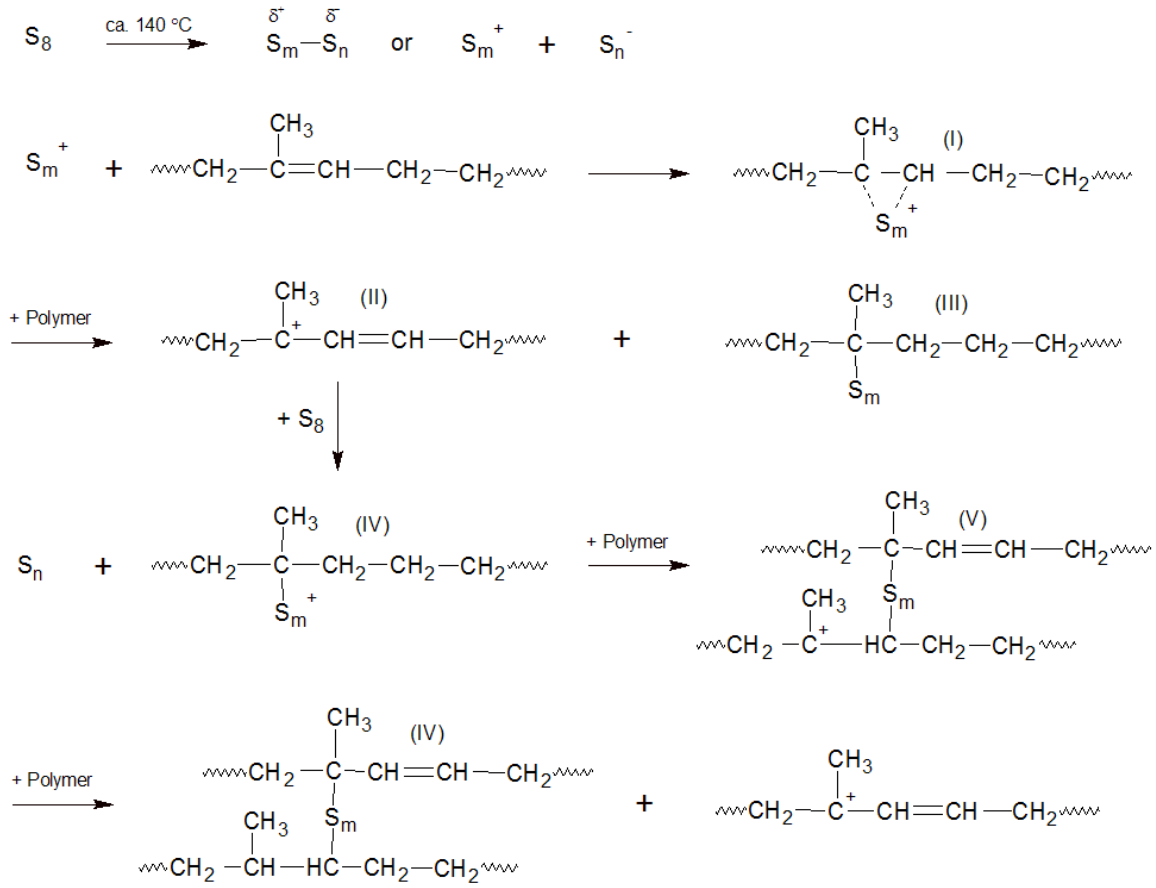

FIG.1. A POSSIBLE REACTION MECHANISM FOR POLYISOPRENE WITH SULPHUR

The polysulfide crosslinks formed by these reactions may contain four to six sulfur atoms at low temperatures whereas at higher reaction temperatures shorter sulfur bridges are formed. Vulcanization of rubber by sulfur alone is extremely slow and can take several hours at elevated temperatures (140°C or more). This is problematic because long exposure to temperature and oxygen leads to oxidative degradation which, in turn, results in poor mechanical properties. It is also not very economical. To minimize rubber degradation and to speed-up the vulcanization process, *accelerators* are usually employed.

Vulcanization of rubber by sulfur alone is an extremely slow process and can take several hours at elevated temperature (140°C or more). This is problematic because long exposure to temperature and oxygen leads to oxidative degradation which, in turn, results in poor mechanical properties [3]. It is also not very economical. To minimize rubber degradation and to speed-up the vulcanization process, accelerators are usually employed. An accelerator is defined as a compound that increases the speed of vulcanization and that enables vulcanization to proceed at lower temperature and with greater efficiency. Accelerator also decreases the amount of sulfur needed to cross-link the polydiene, which improves the aging properties of the vulcanized rubber. Some of the accelerators also function as sulfur donors and thus, allow vulcanization to proceed at lower sulfur content.

The accelerators can be further classified as primary and secondary accelerators. The *primary accelerators* are typically used at 0.5 to 1.5 phr. The vulcanization speed of these systems can range from slow to ultra fast depending on composition and type of accelerator. Common primary accelerators include thiazoles and sulfenamides whereas thioureas and dicarbamates can function as both primary and secondary accelerators. Very fast are *thioureas* and *dicarbamates* (see table below) and semi-fast are *thiazoles* whereas *aldehydeamines* and *guanidines* are rather slow. Some other curatives such as *sulfenamides* are fast curatives and cause a delay in the onset of vulcanization which is often desired in rubber processing because it increases the scorch time. Both the cross-link density and the cure speed depend on the type and dosage of accelerator, or in other words, the number of sulfur atoms in the sulfur bridges, their average number per polymer and the reaction rate depend on the type and composition of the sulfur cure system. Many of the sulfur-based vulcanization systems require activators. For example, dithiocarbamate and thiazole accelerators are activated with *zinc oxide* and *stearic acid* which also increase the speed of vulcanization.

TABLE 1
ACCELERATORS SYSTEM [4]

Compound	Chemical Structure	Side Groups (R)
Guanidine (Moderate)	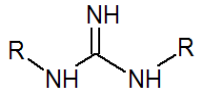	R = Phenyl, Toluoyl R = Alkyl
Dithiocarbamate (Very fast)	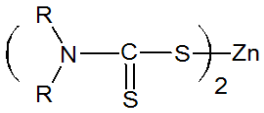	R = Phenyl, Toluoyl R = Alkyl
Thiuram (Very fast)	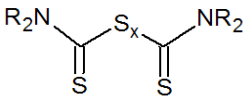	R = Alkyl
2-Mercaptobenzothiazole (Moderate)	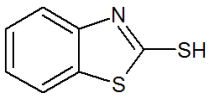	
Zinc-2-mercaptobenzothiazole (Very Fast)	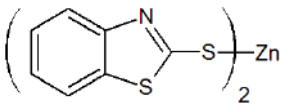	
Thiourea (Very fast)	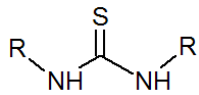	R = Alkyl, Phenyl
Benzothiazole Sulfenamide (Fast - Delayed Cure)	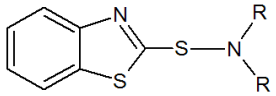	R = H, Alkyl R = Phenyl
Isopropylxanthate (Ultra Fast)	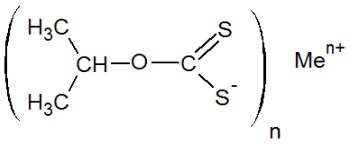	Me^{n+} = Zn^{2+}, Na^{+}

An important factor in the vulcanization process is the cure temperature which also affects the crosslink density and structure. To minimize thermal and oxidative degradation vulcanization should be done at the lowest possible temperature. However, to increase productivity, higher cure temperatures are often chosen. In our study we used the follow vulvanisation's system: sulfur with ZnO, stearic acid and bis (2-benzothiazole) disulfide (MBTS).

III. APPLIED MATERIALS AND METHODS

3.1 Natural Rubber (NR)

Natural Rubber is an elastic substance obtained from the latex sap of trees, especially those trees which belong to the general Hevea Brasiliensis. Technically speaking, natural rubber is an elastomer or an elastic hydrocarbon polymer. Natural rubber is one of the types of rubber that also include vulcanized rubber which is finished into a variety of rubber products. Natural rubber is also known by the names of India rubber, gum elastic, and caoutchouc [4].

The raw material from which natural rubber is made comes from the sap of rubber trees. The rubber plants are tapped for collecting the rubber latex. For this, an incision is made into the bark of the rubber tree and the latex sap is collected in cups.

After collecting the latex sap, the raw natural rubber is refined to convert it into a usable rubber. Initially an acid was added to the latex which used to make the sap set like a jelly. The latex jelly thus obtained was then flattened and rolled into rubber sheets and hung out to dry. In the year 1839, Charles Goodyear invented a more sophisticated way of making rubber stronger and more elastic. This was the process of rubber vulcanising. The unprocessed natural rubber is sticky, deforms easily when warm, and is brittle when cold. In such a state, it cannot be used to make products having a good level of elasticity. Vulcanization prevents the polymer chains from moving independently. As a result, when stress is applied the vulcanized rubber deforms, but upon release of the stress, the product reverts to its original shape.

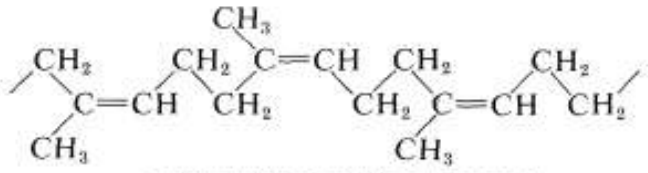

natural rubber (*cis*-1,4-polyisoprene)

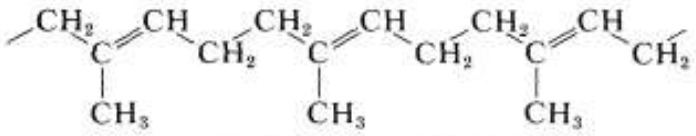

gutta-percha (*trans*-1,4-polyisoprene)

FIG.2. CHEMICAL STRUCTURE OF NATURAL RUBBER (cis-1,4-polyisprene) AND GUTTA PERCHA (trans-1,4-polyisoprene) [5]

3.2 Vulcanisation's system

3.2.1 Sulfur

The cross-linking reaction between sulfur and rubber occurs mainly at the carbon-carbon double bonds (C=C) in large excess of sulfur. Often accelerators are added to speed up the vulcanization and to reduce the amount of free sulfur which has a detrimental effect on the properties of the cured rubber.

3.2.2 Bis (2-benzothiazole) disulfide (MBTS)

The most widely used (primary) vulcanization accelerators are thiazoles. They form sulfur bridges between individual polymer molecules when heated with rubber. Often an initiator is added to accelerate the vulcanization process. This process is rather complicated and involves a sequence of reactions. A possible reaction mechanism for 2-2'-Dithiobis (benzothiazole) (MBTS) accelerated sulfur vulcanization of rubber is shown below. In the absence of an initiator, MBTS reacts with a sulfur molecule (cyclic S8) to form a polysulfide sulfurating agent which then reacts with a rubber unit to form a crosslink precursor and a 2 - mercapto-benzothiazole molecule (MBT). Two of these MBT molecules react to form MBTS again whereas the sulfurated rubber decomposes into a rubber-polysulfide and MBT radical. Assuming a radical mechanism [6], MBT polysulfide radicals combine to form new sufurating agents and/or they react with rubber to form more rubber crosslink precursors whereas the polymeric persulfenyl radicals either combine or react with other rubber molecule to form sulfur bridges, i.e. cross-linked rubber (Figure 3.).

Thiazoles are only medium fast curatives. To increase their cure speed, they are usually combined with small amounts of basic accelerators such as diphenyl guanidine (DPG) or diorthotolyl guanidine (DOTG). These accelerators not only increase the cure speed but also improve scorch delay and crosslink density and thus, improve the mechanical performance of the rubber. Furthermore activators such as ZnO / stearic acid are usually added which further increase the efficiency of sulfur based cure systems and produce flat cure with improved reversion resistance. The activity of an accelerator depends on three major factors: the basicity of the amine, the strength of the sulfur-nitrogen bonds and the concentration of MBTS. The greater the basicity of the amine, the shorter is the scorch delay and the faster is the cure rate. Sterically hindered amines (secondary amines) usually improve scorch safety and result in slower cure. The same is true for more stabilized S-N bonds.

The activity of thiazoles and sulfenamides (and other accelerators) in vulcanization systems also depends on the type of rubber and the vulcanization condition, that is, accelerators can have very different reactivities in different rubber systems and can lead to different crosslink densities [3].

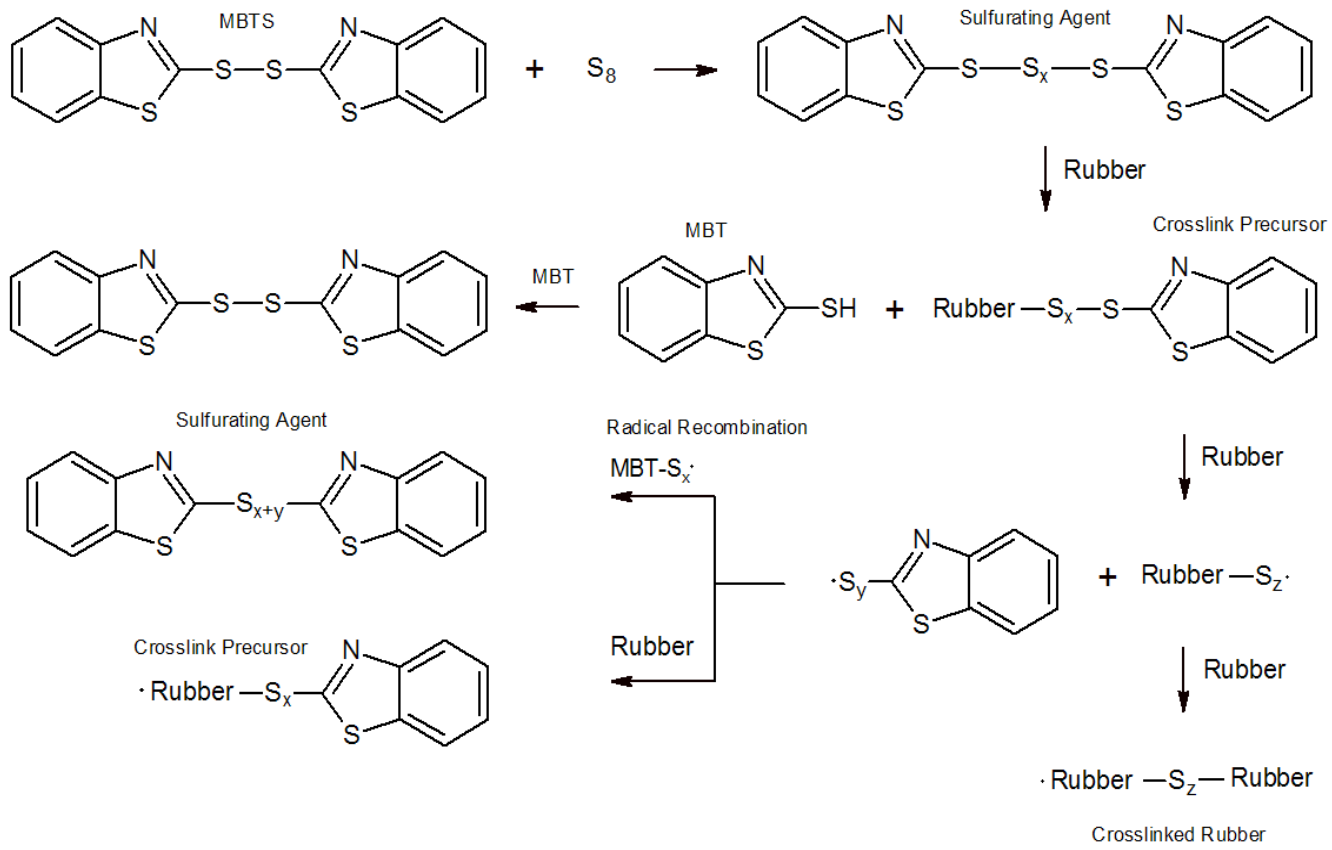

FIG.3.MECHANISM OF MBTS AND Zn CATALYSTS

3.3 Activators for sulfur vulcanization

3.3.1 Stearic acid and ZnO

Typical rubber vulcanization systems consist of rubber, sulfur accelerator, metal oxide and fatty acid, where the last two ingredients represent the activator. They are important rubber processing additives that not only activate cure but also improve the efficiency of sulfur based cure systems. In fact, almost all organic accelerators require the addition of an organic activator to achieve the desired cure and end-use properties. The most common activator is zinc fatty acid ester which is often formed in-situ by reaction of fatty acid with zinc oxide. The most common fatty acids include stearic, lauric, palmitic, oleic and naphthenic acid. The fatty acid solubilizes the zinc and forms the actual catalyst [6]. The ZnO can also act as a filler or white colorant in rubber products whereas the fatty acid improves filler incorporation and dispersion by wetting the oxide particles and reducing interfacial tension (wetting agent). The addition of activators in combination with secondary alkaline accelerators also allows for a more controlled onset of cure. The mechanism of zinc catalyzed sulfur vulcanization is very complex and is often not fully understood [7].

The main catalyst is zinc whereas the fatty acid functions as a solubilizing agent for the zinc which forms a complex with sulfur in the accelerator-polysulfide or is covalently bonded to sulfur atoms in the accelerator molecules as shown below. Both the solubility and reactivity increases if the zinc coordinates with an amine or amide, for example with sulfenamide. The chelated amines increase the nucleophilicity of the sulfur in the polysulfide complex and thereby increase the reaction rate of precursor formation. The exact position where zinc complexes in the accelerator complex is often unknown [8]. Three possible structures of a Zn – polythio-bis(benzothiazole) complex are shown below. The position of the zinc in the accelerator complex affects both the reaction path and the product distribution:

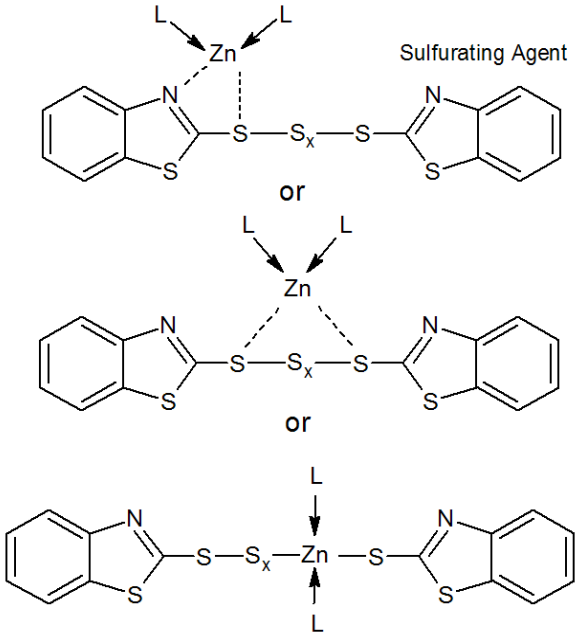

FIG.4. THE ZN-ACCELERATOR COMPLEX [8]

The accelerator complex plays an important role in both the insertion of sulfur atoms into the complex and in the formation of initial polysulfidic crosslinks.[2] As it is the case with other catalysts, remarkable small quantities of solubilized zinc are needed to initiate and speed up the vulcanization process. In the case 2-2'-dithiobis(benzothiazole) (MBTS), the zinc is assumed to complex with the nitrogen atom of a benzothiazole ring [8] as shown below.

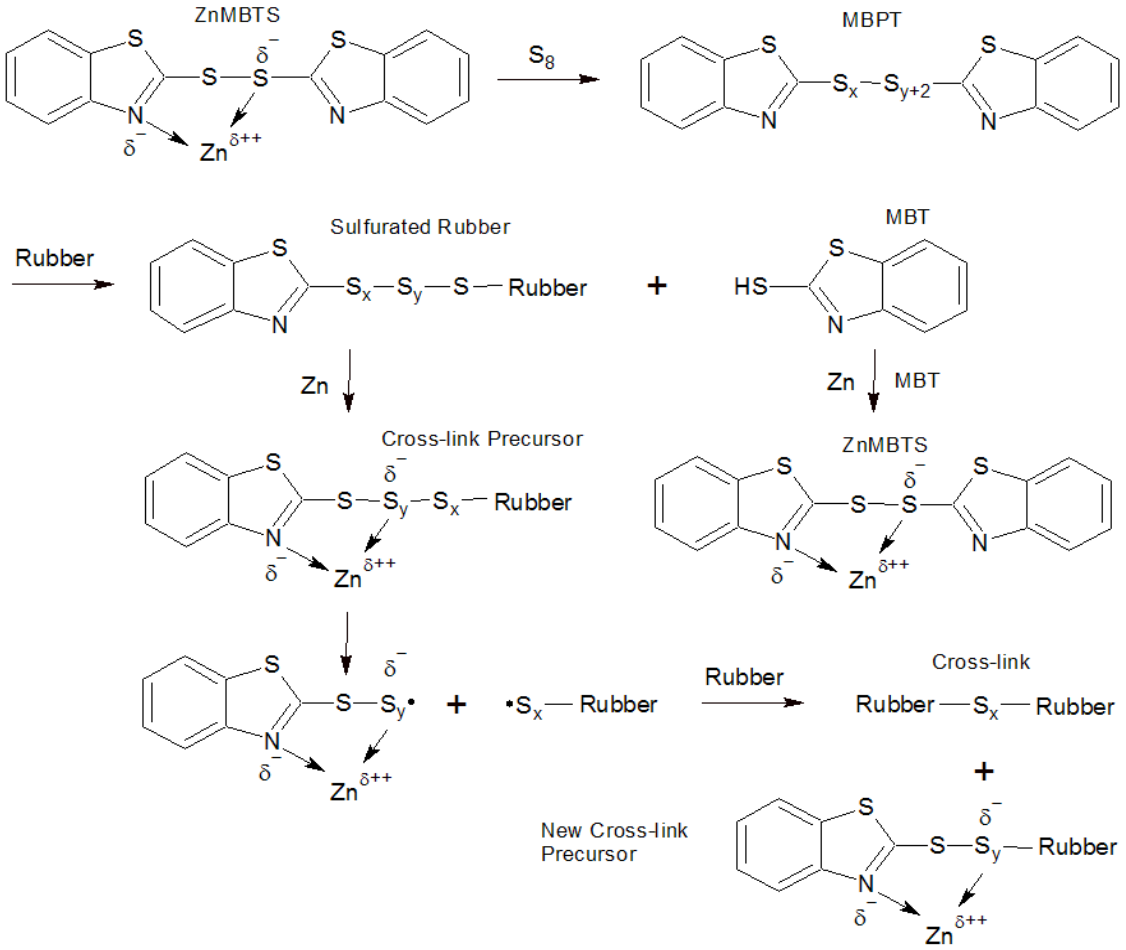

FIG.5. THE COMPLEX WITH THE NITROGEN ATOM OF A BENZOTHIAZOLE RING [8]

The zinc catalyst lowers the energy of dissociation of the sulfur bonds and allows for faster insertion of sulfur molecules (cyclic S8) into the polysulfide sulfurating agent which then reacts with rubber to form a crosslink precursor and 2-mercapto-benzothiazole (MBT). The later reacts with another MBT molecule in the presence of zinc to form another MBTS-zinc complex. Assuming a radical mechanism [8], the cross-link precursor cleaves homolytically into a rubber-polysulfide and polysulfidic benzothiazole radical. The later reacts with rubber to form a new cross-link precursor whereas the polymeric persulfenyl radicals either combine or react with other rubber molecules to form sulfur bridges.

The crosslinks that are formed initially are predominantly polysulfides. During post cure or service life, these polysulfidic crosslinks can degrade (desulfurate) to more stable mono or disulfidic crosslinks which changes the original rubber properties markedly, and/or the polysulfidic crosslinks degrade to elastically ineffective cyclic sulfides or pendant groups. The reaction rate of these post-vulcanization reactions is higher for longer sulfur bridges, since the S-S bonds are weaker when the crosslinks are longer.

3.4 Carbon black

Carbon blacks are mainly used as reinforcing fillers in tire and other rubber products. The reinforcement effect is influenced by the interaction between the elastomer molecules, between the carbon black particles themselves and between the carbon black particles and elastomer matrix also. For elastomer reinforcement, the primary particle size (specific BET surface area) a surface activity of the carbon black types are important as well as their carbon black structure. In addition, the degree of carbon black dispersion achieved and the carbon black loading used in the elastomer composite play a role. The type of carbon black can significantly influence the properties of the resulting rubber compounds. This explains the existence of many different standardized industrial carbon black grades being used in rubber compounds for the body and tread of tires.

Carbon blacks are expected to continue to dominate the rubber market for the foreseeable future, but they are coming under considerable pressure from precipitated silica in some important tire applications. This is because the silica offers lower rolling resistance properties and hence improved fuel economy and lower emissions. This trend is expected to continue to grow.

3.5 Sunflower oil

Plasticizers make it possible to achieve improved compound processing characteristics, while also providing flexibility in the end-use product. Ester plasticizers are selected based upon cost-performance evaluation. The rubber compounder must evaluate ester plasticizers for compatibility, processibility, permanence and other performance properties. They are in production include sebacates, adipates, terephthalates, dibenzoates, gluterates, phthalates, azelates, and other specialty blends. This broad product line provides an array of performance benefits required for the many elastomer applications such as tubing and hose products, flooring, wall-coverings, seals and gaskets, belts, wire and cable, and print rolls. Plasticizer-elastomer interaction is governed by many factors such as solubility parameter, molecular weight, and chemical structure. Compatibility and performance attributes are key factors in developing a rubber formulation for a particular application.

Sunflower oil is a monounsaturated (MUFA)/polyunsaturated (PUFA) mixture of mostly oleic acid (omega-9)-linoleic acid (omega-6) group of oils. The oil content of the seed ranges from 22% to 36% (average, 28%): the kernel contains 45–55% oil. The expressed oil is of light amber color with a mild and pleasant flavor; refined oil is pale yellow. Refining losses are low and the oil has good keeping qualities with light tendency for flavor reversion. The oil contains appreciable quantities of vitamin E, sterols, squalene, and other aliphatic hydrocarbons [9, 10].

TABLE 2
COMPOSITIONS OF MASTER BATCH FORMULATIONS

Material	Weight [g]				
	Sample 1.	Sample 2.	Sample 3.	Sample 4.	Sample 5.
NR	152,00	152,00	152,00	152,00	152,00
Stearic acid	4,55	4,55	4,55	4,55	4,55
Carbon black	76,00	76,00	76,00	76,00	76,00
ZnO	7,60	7,60	7,60	7,60	7,60
MBTS	0,91	1,82	2,74	3,65	4,56
Sulphur	3,80	7,60	11,40	15,20	19,00
Sunflower oil	30,00	30,00	30,00	30,00	30,00

The parameters of mixing procedure were the follow: the vulcanisation's temperature at 145°C, pressure at 220 bar during 10 minutes. The amount of sulfur and MBTS were increased proportionally (show Table 2.).

Base mixtures of NR, carbon black, antioxidant, zinc oxide and stearic acid were prepared in a Banbury internal mixer with a rotor speed of 65 rpm. Curatives were added on an open two-roll mill in a second stage mixing. The base mixes were then crossblended using a masterbatching technique to ensure uniform dispersion of the ingredients and to minimise between-mix variations. The termo-mechanical and optical properties of the mixtures were examined by a Short A hardness tests; DSC (differential scanning calorimetry) and a SEM (scanning electron microscope) instruments. The next chapter contains the results of them.

IV. RESULTS AND CONCLUSION

The Shore A hardness test of the rubber samples containing different Sulphur showed was a significant difference between Sample 1 and Sample 5. (Fig. 6.). The results demonstrate the influence of sulphur and MBTS during the different stages of the vulcanization. With sulfur present, the crosslinked product distribution is influenced as well.

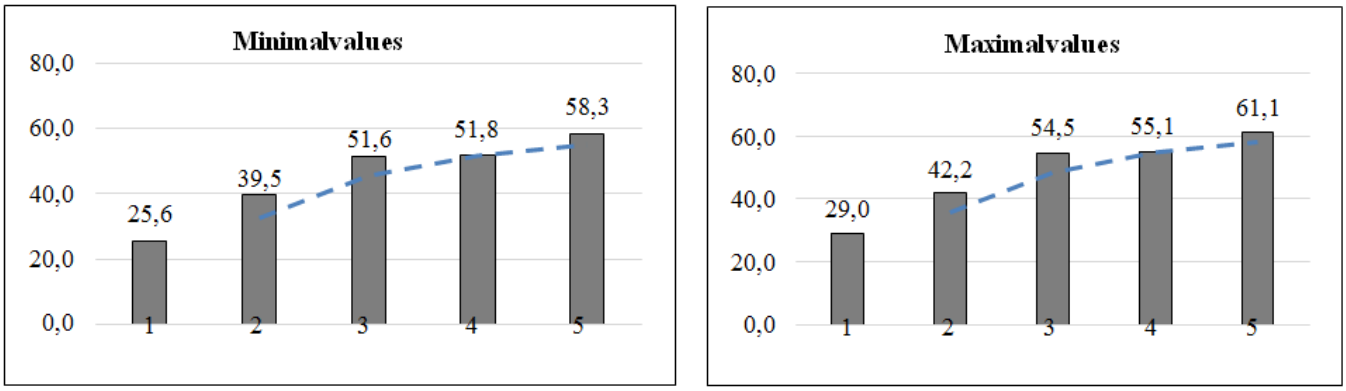

FIGURE 6. a.) THE MINIMAL AND b.) MAXIMAL VALUES OF SHORE A HARDNESS TEST

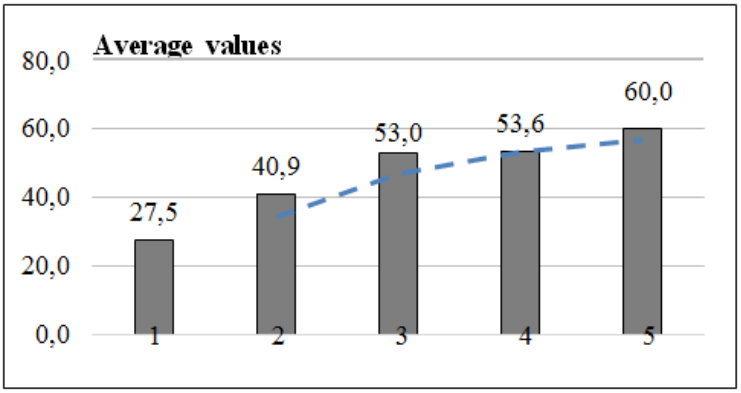

FIGURE 7. THE AVERAGE VALUES OF SHORE A HARDNESS TEST

NR-based master batches, even when similarly compounded, exhibit different cure behavior and cure properties depending on the cure system used, the duration and temperature of cure. The results of DSC tests show that the difference between the samples (Fig.8.). **DSC** (differential scanning calorimetry), is a thermoanalytical technique in which the difference in the amount of heat required to increase the temperature of a sample and reference is measured as a function of temperature. Both the sample and reference are maintained at nearly the same temperature throughout the experiment.

Differential scanning calorimetry can be used to measure a number of characteristic properties of a sample. Using this technique it is possible to observe fusion and crystallization events as well as glass transition temperatures Tg. DSC can also be used to study oxidation, as well as other chemical reactions. In this case we checked the process of vulcanization.

Generally, the temperature program for a DSC analysis is designed such that the sample holder temperature increases linearly as a function of time (from +60°C to +180°C). The cross-linking of polymer molecules that occurs in the curing process is exothermic, resulting in a positive peak in the DSC curve that usually appears soon after the glass transition. The reference

sample should have a well-defined heat capacity over the range of temperatures to be scanned. We collected the results below.

TABLE 3
THE RESULTS OF DSC MEASUREMENTS

Sample ID	Color of curve	Glass-transition temperature [°C]	Heat capacity[J/g]
Sample 1.	purple	116,74	-1,89
Sample 2.	red	116,15	-1,01
Sample 3.	green	120,52	-1,41
Sample 4.	claret	119,03	-1,10
Sample 5.	orange	115,43	-1,28

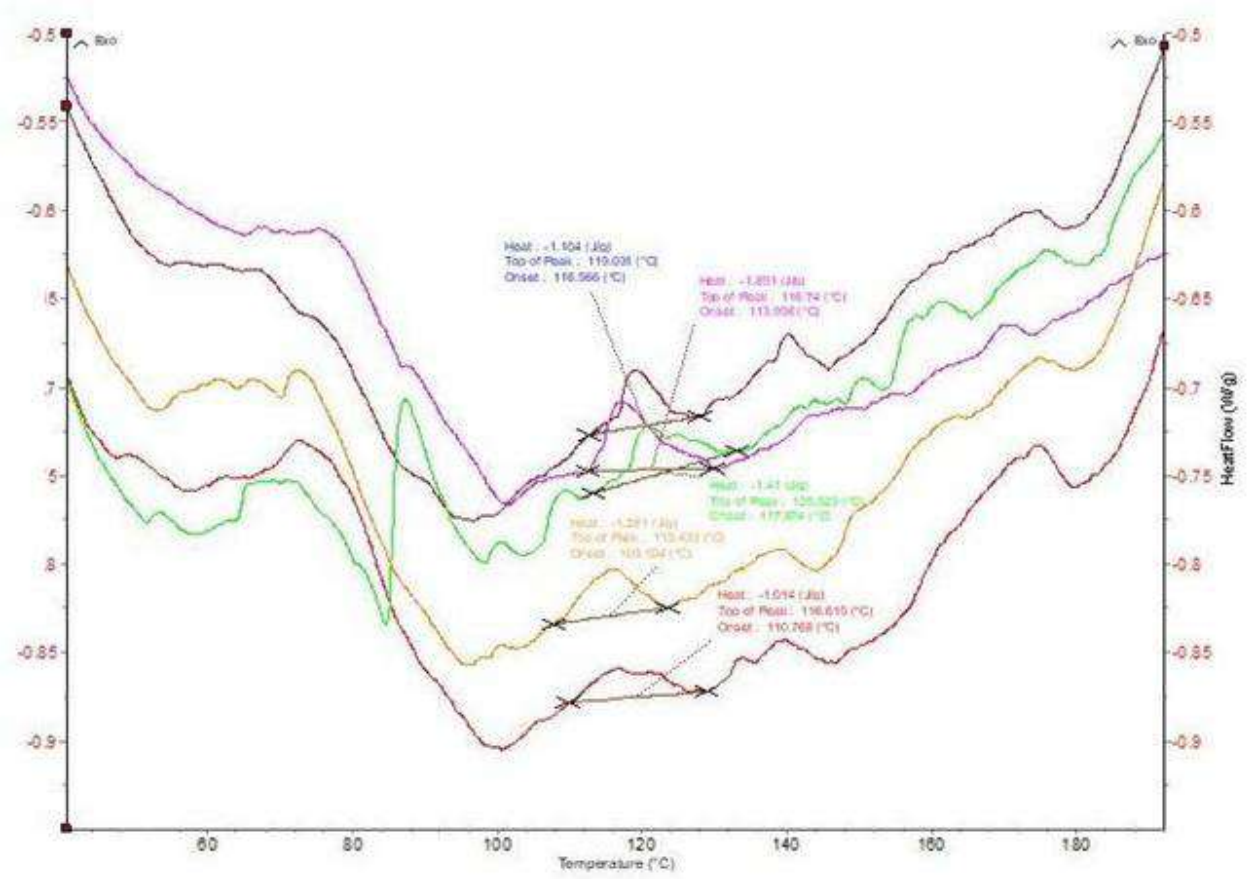

FIGURE 8. THE DSC CURVES OF THE SAMPLES

The aim of the **SEM** investigation was the examination of blending of raw caoutchouc and rubber mixtures (base polymer with additives) in 50x and 1000x magnification. It is evident, that besides the surface impurities, Sample 3. and Sample 5. generated a lot of sulfur aggregation from the vulcanising agent used based on the recipe.

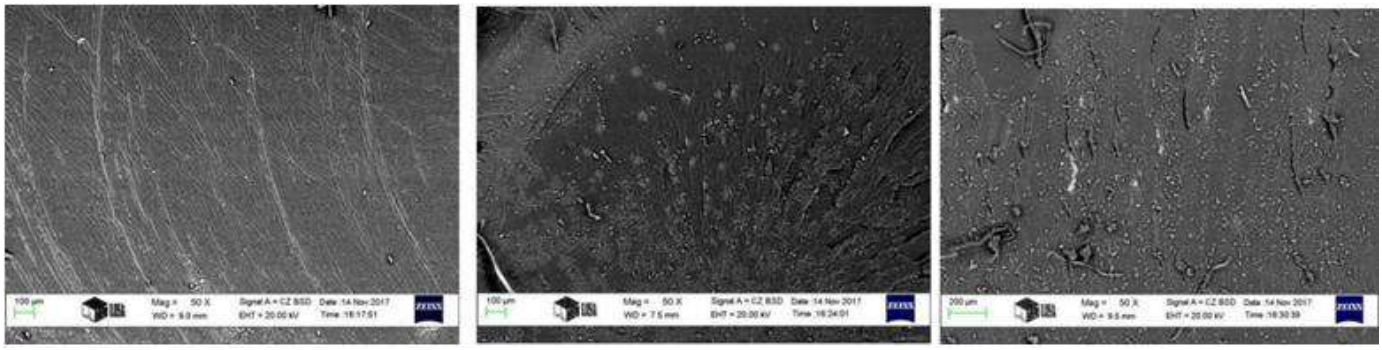

FIGURE 9. THE SEM RESULTS OF a.) SAMPLE 1., b.) SAMPLE 3. AND c.) SAMPLE 5. IN 50x MAGNIFICATION

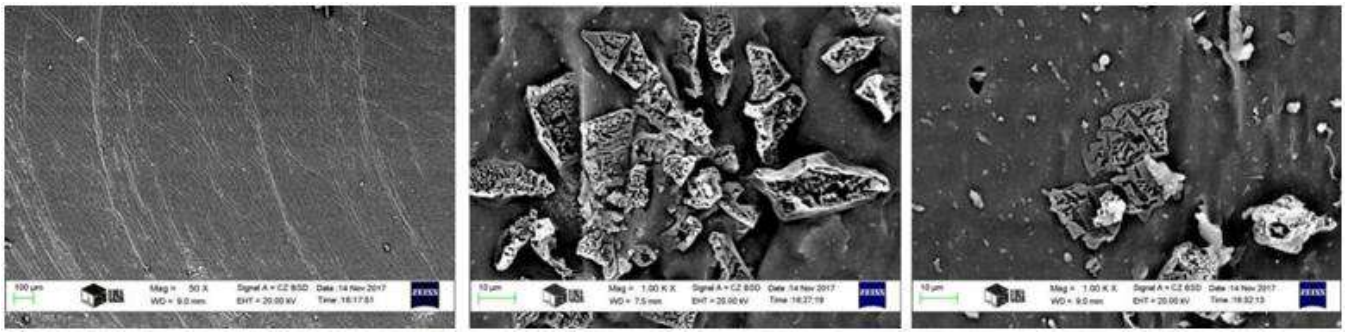

FIGURE 10. THE SEM RESULTS OF a.) SAMPLE 1., b.) SAMPLE 3. AND c.) SAMPLE 5. IN 1000X MAGNIFICATION

ACKNOWLEDGEMENTS

I owe thanks to my supervisor, Gabriella Zsoldos for her support and "Supported by the Únkp-2017-3. New National Excellence Program of the Ministry of Human Capacities".

REFERENCES

[1] P. J. Flory, „Principles of Polymer Chemistry" 1st ed., Cornell University, 1953, pp. 454-464.

[2] A. Oae, *Organic Chemistry of Sulfur*, Plenum Press, New York 1977.

[3] A.M. Joseph, B. George, K.N. Madhusoosaban, and R. Alex, „*Rubber Science"*,2015, pp. 28, 82-121.

[4] A.K. Bohwmick, H.L. Stephens, "Handbook of Elastomers" 2rd ed.., NY, Basel: Marcel-Dekker Inc., 2001, pp.3-7.

[5] J. D. Robert, M. C. Caserio, "B*asic Principles of Organic Chemistry",* 2rd ed., W. A. Benjamin, Inc, Menlo Park, CA. ISBN 0-8053-8329-8

[6] P.J. Nieuwenhuizen, A.W. Ehlers, J.W. Hofstraat, S.R. Janse, M.W.F., Nielen, J. Reedijk, and E.-J. Baerends, „*Chem. Eur. Journal.*1988, Vol. 4, No. 9, pp. 1816-1821

[7] P. Ghosh, S. Katare, P. Patkar, J.M. Caruthers, V. Venkatasubramanian, and K.A. Walker, "*Rubber Chem. Technol*."2003, Vol. 76, No. 3, 592-693

[8] A. Y. Coran, in *The Science and Technology of Rubber*, 2005, Ch.7 - *Vulcanization*, pp. 321-366.

[9] *"Sunflower oil production in 2014; Crops processed/Regions/Production quantity (pick list)". United* Nations Food and Agriculture Organization, Statistics Division (FAOSTAT). 2017.

Adhesion characterization of SiO_2 thin films evaporated onto a polymeric substrate

C. Ho[1], A. Dehoux[2], L. Lacroix[3], J. Alexis[4*], O. Dalverny[5], S. Châtel[6], B. Faure[7]

[1,3,4,5]Department of Interfaces and Functional Materials, LGP-ENIT-INP, University of Toulouse, France
[1,2,6,7]Thin Films Group, R&D Physico-Chemistry, Essilor International, France

***Abstract*—** *To ensure good adhesion between a 200 nm thick silicon dioxide layer and a 4.5 µm thick hardcoat polymeric coating, a better understanding of mechanisms of adhesion at this interface is needed. To reach this purpose, focus is placed on two axes: characterizing mechanical properties of materials composing the system and in parallel, finding an applicable and effective method to quantify adhesion. Small dimension of SiO_2 thin film makes it challenging to accurately characterize it. Hence the use of both nano-indentation and AFM to attempt assessment of SiO_2 thin film elastic modulus Ef; taking into account limitations and uncertainty associated with each technique. Elastic modulus of SiO_2 thin film determined by nano-indentation is roughly 50 GPa on a wafer substrate and 15 GPa on a lens substrate. As for AFM, modulus measured is approximately 56 GPa on a wafer substrate and 22 GPa on a lens substrate. This highlights significant influence of substrate for both techniques. Impact on mechanical properties between SiO_2 thin films under different intrinsic stresses was also investigated. Results suggest that higher density of SiO_2 thin film leads to higher elastic modulus.*

To quantify adhesion, micro-tensile and micro-compression tests were performed. Micro-tensile experiments give ultimate shear strengths of hardcoat-substrate interface ranging from 9 to 14 MPa. Values of energy release rates of SiO_2 / Hardcoat, range from 0.1 J/m² to 0.5 J/m², depending on moduli values found on wafer or lens substrate.

***Keywords*— Adhesion, mechanical properties, oxide thin film, polymer substrate.**

I. INTRODUCTION

Ophthalmic lenses are made of plastic polymeric substrates usually coated with functional treatments composed of 5 to 15 layers, ranging from micrometers to nanometers. The first treatment consists of a primer, conferring impact resistance properties to the lens. A hardcoat with nanoparticles, is then deposited on top of this primer, bringing anti-scratch properties to the system. Both primer and hardcoat are within the micrometer scale and are deposited by wet chemical methods. Nanometric anti-reflective stacks are then evaporated onto the hardcoat by vapor deposition technology, to enhance wearers' comfort. Interface quality is essential to ensure stability and durability of ophthalmic multi-layer. In fact, insufficient adhesion between layers causes higher susceptibility to emergence of defects or delamination. Occurrence of these phenomena affects wearers' comfort and has tremendous impact on products' lifetime. Therefore, it is essential to develop a method enabling quantitative assessment of interface quality, which will ultimately enable to ensure high product reliability.

General behavior of whole system must be fully characterized. To reduce the complexity of this characterization, focus is first placed on studying the interface between the anti-reflective stack and the hardcoat. More specifically, this paper centers around the SiO_2 thin film / hardcoat interface, which is particularly sensitive because of mechanical and dimensional contrast between SiO_2 thin film and hardcoat.

This entails studying both materials composing each layer and interface. Interface quality can be evaluated through quantification of adhesion energy. Over 300 adhesion tests are referenced in the literature [1]. Choice of appropriate method to access adhesion is made according to compatibility with system under study, repeatability, ease of implementation, cost effectiveness and representativeness of defects observed in real life versus defects generated by mechanical tests. Techniques commonly used on similar structure - rigid thin film of 200 nm on soft substrate - include Superlayer, Laser adherence test (Lasat), Bulge test, Pull-off test, three-point bending, micro-tensile and micro-compression tests. Superlayer adhesion test [2], consisting in depositing a highly stressed layer on top of interface of interest, is examined. Lau [3] determines interfacial fracture toughness ranging from 12 J/m² to 24.5 J/m² for dry samples of 0.9 µm silica on 20 µm epoxy, using stressed Chrome Superlayer. Several attempts to generate spontaneous delamination of studied SiO_2 thin film using a Zirconium Superlayer were ineffective. This attests a strong adhesion at SiO_2 / Hardcoat interface. Mechanical test generated by acoustic shock wave, Lasat [4], Bulge test [5] were considered but have not been implemented. Indeed, Lasat test involves laser shock wave that is likely to alter soft polymeric substrate and therefore, is inadequate to structure being studied. Bulge test requires etching step which is delicate considering small dimensions at stake. Moreover, presence of similar chemical

elements between thin film and substrate makes selectiveness of etching process even more complex, which makes bulge test hardly applicable on structure under study. Pull-off tests and three-point bending experiments have been performed. Results located weakest interface at SiO_2 thin film / stiffener and SiO_2 thin film / adhesive interface respectively. This exposes challenge of finding appropriate stiffener or adhesive for strong adhesion interface. This is the reason why pull-off tests and three-point bending experiments were not favored. Through micro-tensile experiments, Alexis et al. [6, 7] have shown correlation between talc particles proportion, thermal post-treatments and practical adhesion of NiP-talc on steel. These results suggest that mechanical adhesion of NiP-talc on steel increases as a function of talc particles proportion and thermal post-treatments. Using micro-compression tests, Xue [8] shows emergence of buckles in a 200 nm titanium thin film sputtered on PMMA substrate. Mode I and Mode II toughness of 0.2 J/m^2 and 0.8 J/m^2 respectively, and interface strength of 80 MPa were determined for Ti / PMMA system by finite element simulations. Considering specifications required for choice of adhesion test and preliminary testing, focus was placed on both micro-compression and micro-tensile tests, which seems suitable for system being studied and have the advantage of applying uniaxial stress without mechanical contact in the area under observation.

As mentioned earlier, emphasis is also placed on determining mechanical behavior of each material to obtain a global understanding of the composite system being studied. In fact, regardless of the adhesion test performed, mechanical properties are needed to fully understand fracture energies. More specifically, it is important to quantify contributions of elastic and plastic dissipations, as well as dissipations through friction or fracture, to estimate adhesion at interface as accurately as possible. Nano-indentation [9] is widely used to determine mechanical properties of both bulk materials and thin films deposited on substrate. However, influence of substrate is inevitable for thin films of a couple of nanometers thick. To limit this effect, correction of substrate's influence using FEA exists [10, 11]. Another approach consists in using an alternative technique with better surface detection to enable characterization of the first nanometers of thin film. AFM, one of the best techniques for surface imaging at an extremely high resolution, classically gives topography and surface roughness information. Nevertheless, several studies have used AFM to extract mechanical properties of sample of interest. Elastic modulus can indeed be determined using DMT contact model with slope of retract curve [12, 13]. As mentioned earlier, this alternative method to characterize elastic modulus has the advantage of having higher sensitiveness to surface detection compared to nanoindentation. It also involves a more confined interaction volume, which is expected to lead to a lower impact from the film microstructure or the substrate. However, limitations of mechanical characterization by AFM include sensitiveness to topography, cantilever spring constant and tip contact area uncertainties. In the present study, elastic modulus of SiO_2 thin film deposited on Si wafer and ophthalmic lens substrate are characterized by both nano-indentation and Peak Force AFM. Micro-tensile and micro-compression results to quantify SiO_2 / hardcoat adhesion, are also presented.

II. MATERIALS AND METHODS

2.1 Samples

SiO_2 Type A and SiO_2 Type B are deposited by evaporation under vacuum whether on silicon wafer (280 µm thick and 2 inches diameter wafers) or on top of standard ophthalmic structure: 4.5 µm composite polymer referred to as hardcoat, on a 2 mm polycarbonate substrate. That is a total of four sample configurations, represented in Figure 1. Deposition of both types of SiO_2 layers is conducted under a pressure of 8.10^{-5} to 1.5×10^{-4} mbar [14]. Difference between SiO_2 Type A and B results from supply of gas during deposition: SiO_2 Type A is deposited along with oxygen gas whereas SiO_2 Type B deposition does not involve introduction of additional gas. This difference in process was proven to effectively generate different levels of intrinsic stress within SiO_2 layers, due to increase of porosity related to gas scattering during deposition [15]

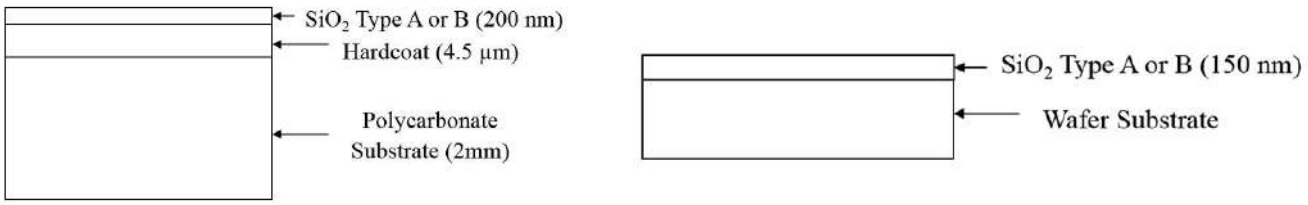

(a) **(b)**

FIG. 1. Representation (not to scale) of sample configurations on lens substrate (a) and silicon wafer substrate (b).

Compressive intrinsic stress of SiO_2 Type on glass strip (60 mm x 5 cm x 150 µm) was measured to be roughly -100 MPa, compared to -400 MPa for SiO_2 Type B. Bending curvature of glass strip was measured before deposition of SiO_2 thin film on KLA Tencor P16+. Glass strip was then placed into evaporation under vacuum chamber (glass strip being only clamped on one end, the other end remaining free) to receive deposition of SiO_2 thin film. Another measurement of glass strip's bending curvature was performed 2 hours after deposition. Compressive intrinsic stresses are then calculated using Stoney's equation [16, 17]. Stoney uses bending curvature of glass strip before and after deposition of SiO_2 thin film.

$$\sigma_f = -E_s \frac{{h_s}^2}{(1-\nu_s)h_f}\frac{1}{R} \tag{1}$$

Where E_s is Young modulus of substrate, h_s and h_f are substrate and film thickness respectively, ν_s is substrate's Poisson coefficient and R is radius of curvature. Presented below are methods used to characterize materials mechanical properties, by nano-indentation and AFM.

2.2 Nano-indentation

Four sample configurations were characterized with a Nanoscope XP III from MTS, using a DCM measuring head and Berkovich diamond tip. A matrix of 30 indents separated by 30 µm, was created for each configuration. Before carrying out nano-indentation tests, tip area was first calibrated with a sample of fused silica. Continuous Stiffness Mode (CSM) which consists in overlapping a small amplitude oscillation at 75 Hz to a load controlled system was used. Using Oliver and Pharr model [9], both elastic modulus and hardness can be extracted directly from nano-indentation curve, plotting load versus displacement into surface.

$$S_e = \frac{2}{\sqrt{\pi}} E_r \sqrt{A(h_c)} \tag{2}$$

Where S_e is contact stiffness determined at the beginning of unloading curve, $A(h_c)$ is contact area as a function of indentation depth and E_r is reduced modulus, expressed as followed:

$$\frac{1}{E_r} = \frac{1-\nu^2}{E} + \frac{1-{\nu_i}^2}{E_i} \tag{3}$$

Where E_i and ν_i are respectively indenter's modulus and Poisson coefficient. A value of 0.18 [18] was taken as silica thin film's Poisson coefficient.

2.3 AFM

Four sample configurations were characterized by AFM using Peak Force QNM mode on a Bruker's Dimension Icon. AFM tip radius has been calibrated using fused silica of known elastic modulus. Cantilever's spring constant of 436 N/m has been given by tip provider. Cantilever with high spring constant has been chosen for its suitability to hard materials. Several Peak Force values have been tested to determine the optimal Peak Force to apply on this specific sample. Using DMT model [19, 20], elastic modulus can be determined with slope of retract curve, Poisson coefficient of film, radius of indenter R and indentation depth δ.

$$F - F_{adh} = \frac{4}{3}\frac{E}{\left(1-\upsilon^2\right)}\sqrt{R}\,\delta^{\frac{3}{2}} \tag{4}$$

Second part of this study involves characterization of practical adhesion of SiO_2 / Hardcoat interface, by micro-tensile and micro-compression test.

2.4 Micro-tensile Test

Micro-tensile test is commonly used to determine material's elasticity, plasticity and toughness properties. Applying Agrawal and Raj's model [21, 22], micro-tensile test can also be used as an adhesion test to determine ultimate shear strength of the interface.

SiO_2 Type A and SiO_2 Type B deposited on top of standard ophthalmic structure were tested. Although interface of interest is SiO_2 / Hardcoat, small dimension of hardcoat hinders testing the bilayer system by itself; hence the use of a 2 mm thick

polymeric substrate to support this structure. Typical tensile specimen was designed, with optimized shoulders and gage length, (Figure 2) to fit Deben's micro-tensile stage (5kN tensile compression and horizontal bending stage) and allow sufficient observation area. Samples were precision machined on a Charly Robot milling machine, with a 2 mm diameter milling cutter.

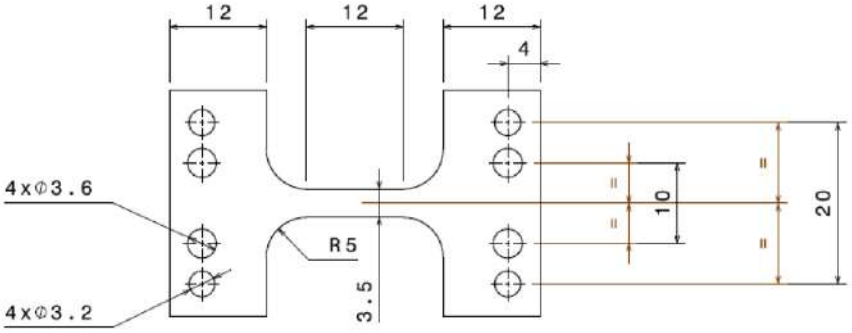

FIG. 2. Representation of tensile specimen

High crack density is associated with good mechanical strength, resulting in higher values of maximal interfacial shear stress τ. Agrawal and Raj [21] relate maximal interfacial shear stress τ with coating thickness, sum of true stress and residual stress σ and maximum cracking spacing λ, when crack density becomes constant.

$$\tau = \frac{\pi h \sigma}{\lambda} \tag{5}$$

2.5 Micro-Compression Test

Configuration of SiO_2 Type B on lens structure sample was tested. Micro-compression tests were performed on the same Deben stage with a 5 kN load cell, used under compression mode. Motor speed was set to 0.2 mm/min. Preliminary tests were performed to estimate minimum deformation of substrate to generate buckling on sample SiO_2 B. 10% deformation and stress of 100 MPa have been proven to be sufficient to buckle studied SiO_2 thin film. Dimensions (Length: 15 mm, Width: 5 mm, Thickness: 2 mm) were then optimized by analytical calculations to avoid flexural buckling of substrate at applied loads, and thus ensuring uniaxial compressive stress. The critical compressive biaxial stress at the onset buckling is expressed as followed:

$$\sigma_{B0} = \frac{\pi^2}{12} \frac{E_f}{1-\nu^2} \left(\frac{h}{b}\right)^2 \tag{6}$$

Where h is thickness of film, is b is half width of buckle and E_f is plane strain moduli of film [23]. Energy release rate G along the sides of the buckle can be estimated by studying on one hand, the average energy per area in the unbuckled state U0 and on the other hand, the average energy per area in the buckled state U, through the relation: $G = U_0 - U$. Expressed differently the energy release rate G is the energy per area needed to separate SiO_2 thin film from substrate over the width of buckle and is defined as [23]:

$$G = G_0 \left(1 - \frac{\sigma_{B0}}{\sigma_0}\right)^2 \tag{7}$$

with G_0, the available energy per area stored in the unbuckled film:

$$G_0 = \frac{(1-\nu_f{}^2)\sigma_0^2 h}{2E_f} \tag{8}$$

With σ_0, the biaxial compressive stress in the buckled plate.

III. RESULTS AND DISCUSSION

3.1 Nano-hardness and rigidity

As shown in Figure 3a, modulus of hardcoat is measured to be between 6 – 7 GPa by nano-indentation. It can be noted that modulus is relatively stable over a wide range of indentation depths; except for the first 10 nm, where surface detection can

be particularly sensitive on a composite polymer. On the contrary, rapid evolution of modulus of SiO_2 thin film as a function of displacement into surface is observed.

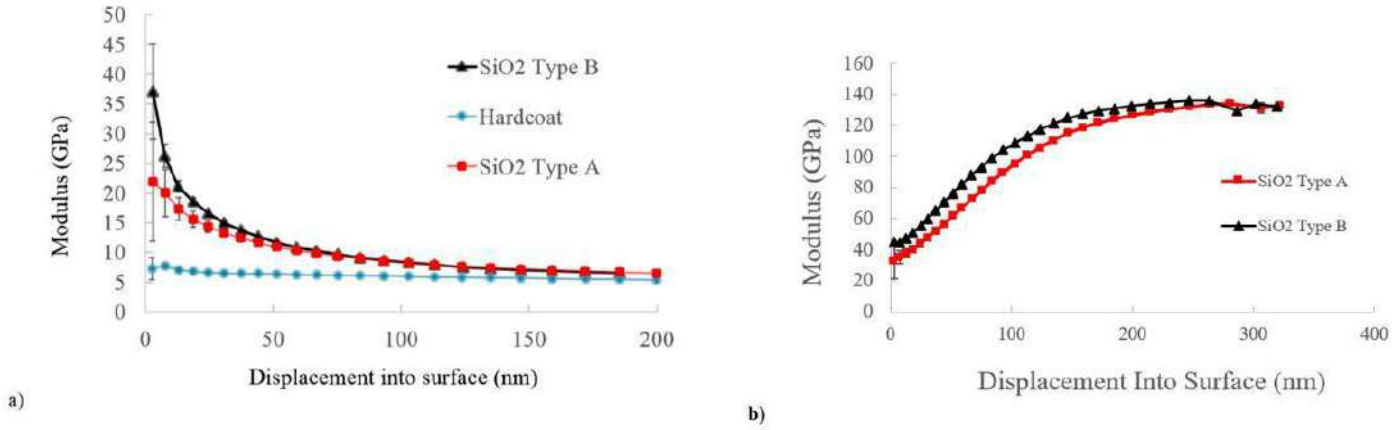

FIG. 3. Representation of their moduli as a function of displacement into surface. (a) Nano-indentation results of Hardcoat, SiO_2 Type A and B deposited on Hardcoat (b) Nano-indentation results of SiO_2 Type A and B on Silicon Wafer

This confirms that substrate's influence has a considerable impact on SiO_2 thin film's modulus measurement. Models to correct substrate's impact relying on FEA to precisely determine contact radius, have not been implemented as it requires mechanical properties of material to characterize. It should be noted that moduli obtained for indentation depths below 20 nm are susceptible to surface detection errors. Above 30 nm indention depth, substrate's influence becomes significant. Moduli are therefore averaged for indentation depths between 20 and 30 nm, even though influence of substrate is already existent and acknowledged (Table 1).

TABLE 1
ELASTIC MODULI OF SiO_2 TYPE A AND B DEPOSITED ON WAFER AND ON OPHTHALMIC LENS, OBTAINED BY NANO-INDENTATION

Substrate	Young Modulus (GPa) SiO_2 A	Young Modulus (GPa) SiO_2 B
Silicon Wafer	46±2	5±1
Ophthalmic lens (hardcoat on Polycarbonate)	14±1	17±0

On both Si wafer and lens substrates, SiO_2 Type A and B are differentiable. Modulus of SiO_2 Type B is 26% higher than modulus of SiO_2 Type A on Si wafer. The same trend is observed for lens substrate, difference being slightly lower (16%). This suggests that the change of material density leads to a higher intrinsic stress and also to the modification of mechanical properties. This is in good agreement with the fact that intrinsic stress is linked to local density – without porosity taken into account - through Si-O-Si deformation; diminution of bond angle at the O atom site, being related to increase in intrinsic stress [15]. Moduli of SiO_2 thin film measured on Si wafer are significantly higher (~250%) than those on lens. According to curves presented on Figure 3, elastic moduli of SiO_2 are overestimated on Si wafer and underestimated on lens substrate. Aside from contribution of substrate's influence, outgassing of lens substrate may explain lower moduli compared to those found on Si wafer. Moreover, during deposition, thermal stress could be generated on polymer substrate due to heat load of electron beam. Given that coefficient of thermal expansion of SiO_2 and polymer are significantly different, this may result in change of dimension of polymeric substrate, which might ultimately impact SiO_2 modulus value. Even though this range is extremely wide, we can conclude that true value SiO_2 lies somewhere between 14 GPa and 46 GPa for SiO_2 Type A and between 17 GPa and 58 GPa for SiO_2 Type B. Scherer [15] determined moduli of 120 nm SiO_2 thin film on glass substrate to be between 35 GPa and 48 GPa (SiO_2 deposition by electron-beam evaporation involving introduction of oxygen gas). This is within the range of moduli found for SiO_2 Type A, taking into account standard deviations. Characterization of mechanical properties by AFM were performed using a Peak Force value of 1000 nN, which has been chosen to have a deformation value around 2 nm. Results are summarized in Table 2.

TABLE 2
ELASTIC MODULI OF SiO_2 TYPE A AND B DEPOSITED ON WAFER AND ON OPHTHALMIC LENS, OBTAINED BY AFM

Substrate	Young Modulus (GPa) SiO_2 A	Young Modulus (GPa) SiO_2 B
Silicon Wafer	48±9	64±14
Ophthalmic lens (hardcoat on Polycarbonate)	22±3	23±3

Mean values are calculated for the four sample configurations from 262144 (512x512) approach-retract curves. Modulus of SiO_2 Type B is 33% (48 ± 9 GPa) higher than modulus of SiO_2 Type A (64 ± 14 GPa) on Si wafer when modulus of SiO_2 Type B is 5% (22 ± 3 GPa) higher than modulus of SiO_2 Type A (23 ± 3 GPa) on polymeric lens substrate. Taking into account the high standard deviations values, moduli of SiO_2 A and B on each substrate, could be considered similar. The high standard deviations on moduli values could come from topographic crosslink modifying the effective contact area, resulting in erroneous calculi from DMT model. Roughness (Ra) of SiO_2 film on Si wafer were measured around 2 nm. Topographic cross link remains under study as well as possible mechanical heterogeneities existing in the films at the nanometric scale. On the other hand, SiO_2 moduli on silicon wafer are significantly higher than SiO_2 moduli on ophthalmic lens. This suggests that moduli of thin film are still impacted by substrate, even though deformation depth was found to be roughly 2 nm. Hypothesis can be made on AFM tip's oscillation at 2 kHz, which may affect behavior of viscoelastic hardcoat underneath SiO_2 thin film on lens structure, causing differences observed on moduli between the two substrates.

3.2 Mechanical Adhesion of thin film

3.2.1 Determination of interfacial shear stress by micro-tensile test

Presented on Figure 4 is a Scanning Electron Micrograph of fractured tensile specimens. Inter-crack spacing is clearly defined and averaged over 15 measurements before computing it into Agrawal and Raj's model. Interfacial shear stress ranges from 9 to 14 MPa, due to variability in first cracking occurrence determination and steady state determination

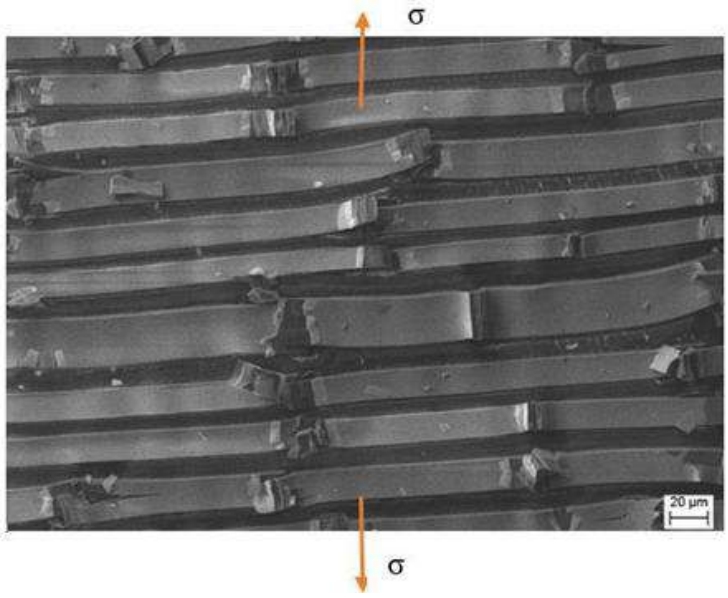

FIG. 4. Scanning Electron Micrograph of fractured tensile specimen

EDS analyses were performed on fractured areas to determine at which interface cracking occurred (Figure 5). Large quantity of carbon in areas where interface is released indicates polycarbonate substrate is underneath cracked layer. This suggests that interface characterized is hardcoat / substrate. Given that SiO_2 thin film is more rigid than underlying hardcoat, it is likely that cracking of SiO_2 appeared before cracking of hardcoat. This seems to indicate that first visible cracking under SEM, occurs in the hardcoat. Characterization under other optical methods which may allow better detection of cracking of SiO_2, will be tested.

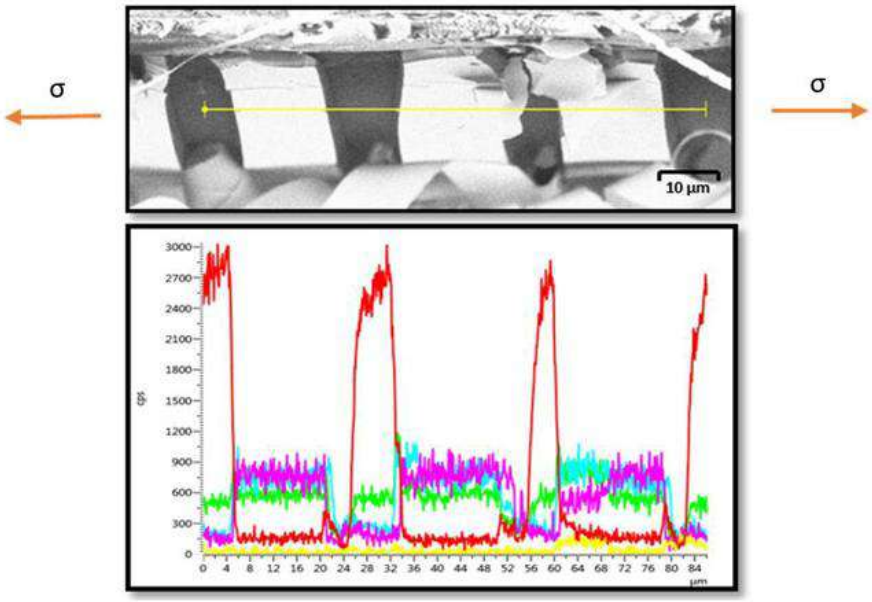

FIG. 5. Scanning Electron Micrograph of delaminated area after micro-tensile test (top image) with EDS profiles over delaminated area: Carbon (red), Oxygen (Green) and Silicon (blue). (bottom image).

3.2.2 Determination of critical stress for onset buckling by micro-compression test

Initiation and instantaneous propagation of buckles, as well as cracking, were observed during application of compressive stress on SiO_2 Type B on lens sample. During the relaxation phase, straight-sided buckles progressively convert to telephone cords morphologies [25]. Concomitance of buckling and cracking (Figure 6) during testing can be explained with hypothesis on mechanisms of their initiations. It is assumed that given sufficient energy, initiation of buckling, followed by its widening, seems to be the logical sequence of events. However, in areas where adhesion is stronger, buckle enlargement seems more difficult than growth of buckle height. This is likely to generate important bending curvatures that eventually lead to cracking. Therefore, we can formulate the hypothesis that occurrence of buckle or cracking can give information on adhesion at a very local level. Ratio of buckles to cracks populations was estimated to be approximately 2 over an observation area of 1.7 x 2.3 mm². Half-width of uncracked buckles averaged over 15 measurements is b = 18±2 µm. This gives values of energy release rates ranging from 0.1 J/m² to 0.5 J/m², depending on moduli values found on wafer or lens substrate. This is within the range of adhesion energies found in the literature, for example, 0.8 to 1.2 J/m² for Au on PI [8]. During relaxation, edges of buckle tend to flatten and end up resting on surface. As relaxation goes on, longitudinal buckle evolves into telephone cord morphology as shown in Figure 7.

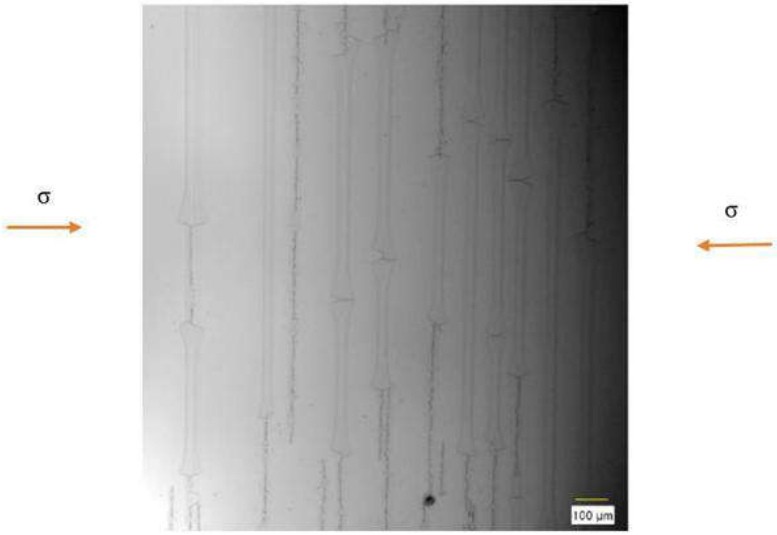

FIG. 6. Optical Microscope observation of buckles and cracks after micro-compression tests. Concomitance of buckles and cracks (x 5). Buckles and transverse cracks (x 20).

Height of buckle under stress could not be measured because in-situ high-resolution topography measurement technique has not been implemented yet. However, height of telephone cord observed in post-mortem specimen was estimated to be 2.2 µm (Figure 7). Identification of layer that buckles has been made on a specimen where telephone cords have been removed by tape, in order to release the interface. Step height of delaminated areas, identified with AFM, was found to be 200 nm which corresponds to thickness of SiO_2. Profile analysis of chemical composition over a delaminated area shows increased quantity of silicon and oxygen and decreased quantity of carbon on higher zones. These analyses strongly suggest delamination at the SiO_2 / Hardcoat interface and support validation of micro-compressive testing as an effective adhesion test to solicit interface of interest.

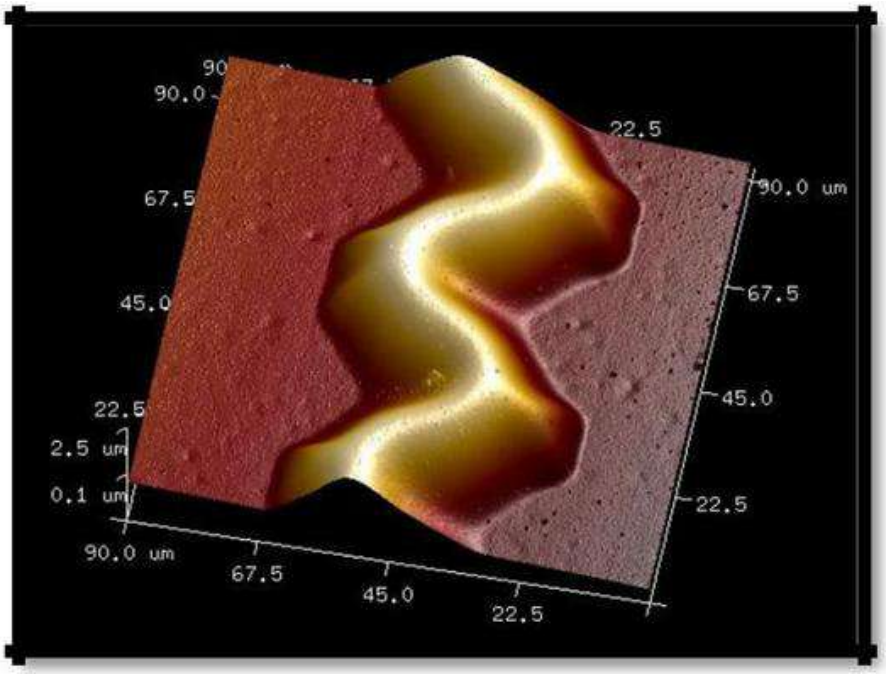

FIG. 7. Telephone cord morphology observed during relaxation of compressive stress, obtained by AFM

IV. CONCLUSION

Elastic moduli of SiO_2 Type A and B were determined by nano-indentation, giving results ranging between 46 and 58 GPa for Si wafer substrate and 14 and 17 GPa for polymeric lens substrate. Same measurements were carried out using AFM. Moduli found are 48 and 64 GPa for Si wafer substrate and 22 and 23 GPa for polymeric lens substrate. Modulus of SiO_2 Type B was found to be roughly 20% higher than SiO_2 Type A, by nano-indentation. Regarding the high standard deviation of moduli measured by AFM, no significant difference between elastic moduli of SiO_2 Type A and B was observed by AFM on both substrates. However, an important difference between moduli of SiO_2 on lens and on Si wafer was observed. This exposes unexpected influence of substrate on mechanical measurements using AFM, which has been hypothetically attributed to impact of Peak Force high frequency oscillations on viscoelastic substrates. Adhesion characterization by micro-tensile experiments gives ultimate shear strengths of interface hardcoat-polycarbonate substrate ranging from 9 to 14 MPa. Detection of cracking of SiO_2 on hardcoat is ongoing. EDX profiles over delaminated area obtained by micro-compressive tests, strengthen the hypothesis that delamination occurred at the interface of interest. This gives values of energy release rates ranging from 0.1 J/m² to 0.5 J/m², depending on moduli values found on wafer or lens substrate. Repeatability and reproducibility studies are undergoing to fully validate this adhesion test. Future immediate perspectives include comparison of energy release rates G for different configurations of SiO_2 thin film. Broader perspectives consist of simulating the micro-compressive adhesion test. Simulation is indeed the only method known to access information such as plastic dissipation or deformation, allowing better analysis of adhesion test

ACKNOWLEDGEMENTS

Financial support for the conduct of this research was provided by Essilor International. The authors would like to acknowledge P. Calba's Materials Advanced Characterization team at Essilor International for their technical support. The authors are also grateful to Bruker's Nano-Surface Division team for performing characterization of moduli by AFM, using PF-QNM on Dimension Icon.

REFERENCES

[1] K.L. Mittal, Adhesion measurement of films and coatings: a commentary, in K.L. Mittal (Eds.), Adhesion measurement of films and coatings, (1995), 1–13.

[2] J. Zheng, S.K. Sitaraman, Fixtureless Superlayer-driven delamination test for nanoscale thin-film interfaces, Acta Materiala. 50 (2002) 441-466.

[3] D. Lau, K. Broderick, M. J. Buehler, and O. Buyukozturk, A Robust Nanoscale Experimental Quantification of Fracture Energy in a Bilayer Material System, Proceedings of the National Academy of Sciences 111, 33 (2014) 11990–11995.

[4] S. Barradas, M. Jeandin, C. Bolis, L. Berthe, M. Arrigoni, M. Boustie, & M. Barbezat, Study of adhesion of PROTAL® copper coating of Al 2017 using the laser shock adhesion test (LASAT). Journal of Materials Science, 39(8), (2004), 2707-2716.

[5] Y. Xiang, X. Chen, and J.J. Vlassak, Plane-strain bulge test for thin films. Journal of materials research 20.09 (2005): 2360-2370.

[6] J. Alexis, C. Gaussens, B. Etcheverry & J. P. Bonino, Development of nickel–phosphorus coatings containing micro particles of talc phyllosilicates. Materials Chemistry and Physics, 137(3) (2013) 723-733.

[7] J. Alexis, C. Gaussens, B. Etcheverry, J-P. Bonino, Development of nickelephosphorus coatings containing micro particles of talc Phyllosilicates, Materials Chemistry and Physics 137 (2013) 723-733.

[8] X. Xue, S. Wang, H. Jia, C. Zheng, H.Bai, Z. Wang, Buckling delamination and cracking of thin titanium films under compression: Experimental and numerical studies, Surface and Coatings Technology, 244 (2014) 151-157.

[9] G.M. Oliver, W.C. Pharr, Improved technique for determining hardness and elastic modulus using load and displacement sensing indentation experiments. Journal of Materials Research, 7 6 (1992) 1564-1583.

[10] H. Li & J. J. Vlassak, Determining the elastic modulus and hardness of an ultra-thin film on a substrate using nanoindentation. Journal of Materials Research, 24(03) (2009) 1114-1126.

[11] J. Hay & B. Crawford, Measuring substrate-independent modulus of thin films. Journal of Materials Research, 26(06) (2011) 727-738.

[12] J. Hopf & E.M. Pierce, Topography and mechanical property mapping of International Simple Glass surfaces with atomic force microscopy. Procedia Materials Science, 7, (2014) 216-222.

[13] P. Trtik, J. Kaufmann, U. Volz, On the use of peak-force tapping atomic force microscopy for quantification of the local elastic modulus in hardened cement paste, Cem. Concr. Res., (42) 1 (2012) pp. 215–221.

[14] P. Roisin, Method for producing an optical article coated with an antireflection or a reflective coating having improved adhesion and abrasion resistance properties, US 8318245 B2 (2012).

[15] K. Scherer, Optical and mechanical characterization of evaporated SiO_2 layers. Long-term evolution, Applied Optics, 35 25, (1996) 5067 – 5072.

[16] G. Stoney, The tension of metallic films deposited by electrolysis, Proceedings of The Royal Society A: Mathematical, Physical and Engineering Sciences, 82 553, (1909) 172-175.

[17] M. Ohring, Materials Science of Thin Films, Second Edition, Elsevier Science, 2001.

[18] J. Barbe, Procédé pour contraindre un motif mince, EP 1615271 B1 (2010).

[19] V. Derjaguin, V. M. Muller et Yu. P. Toporov, Effect of Contact Deformations on the Adhesion of Particles, Journal of Colloid and Interface Science, 53 2 (1975) 314–326.

[20] D. Maugis, Contact Adhesion and Rupture of Elastic Solids, Springer-Verlag Berlin Heidelberg, 2000.

[21] D.C. Agrawal and R. Raj, Measurement of the ultimate shear strength of a metal-ceramic interface, Acta metall., 37 4 (1989) 1265-1270.

[22] Y. Balcaen, N. Radutoiu, J. Alexis, J.-D. Beguin, L. Lacroix, D. Samélor, C. Vahlas, Mechanical and barrier properties of MOCVD processed alumina coatings on Ti6Al4V titanium alloy, Surface and Coatings Technologies, 206 7 (2011) 1684-1690.

[23] M-W. Moon et al. Buckle delamination on patterned substrates. Acta Materialia 52.10 (2004): 3151-3159.

AD Publications
Sector-3, MP Nagar, Bikaner,
Rajasthan, India
www.adpublications.org, info@adpublications.org